Electronic Supplementary Material (ESI) for Catalysis Science & Technology.

Supporting Information

The effect of the zeolite environment on the stability of butene cracking intermediates

Pieter Cnudde, Michel Waroquier, Veronique Van Speybroeck*

Center for Molecular Modeling, Ghent University, Technologiepark 46, 9052 Zwijnaarde, Belgium

* Corresponding author: Veronique.vanspeybroeck@ugent.be

Table of Contents

S1. Zeolite models

All calculations in this study are performed on a fully periodic zeolite model to properly account for the confinement of the zeolite pores. Each zeolite framework contains a single Brønsted acid site per simulation cell, which is created by substitution of a Si atom by an Al atom and adding a charge-compensating proton. An overview of the investigated topologies can be found in **Table S1** and a schematic representation of the topologies is shown in **Figure S1**.

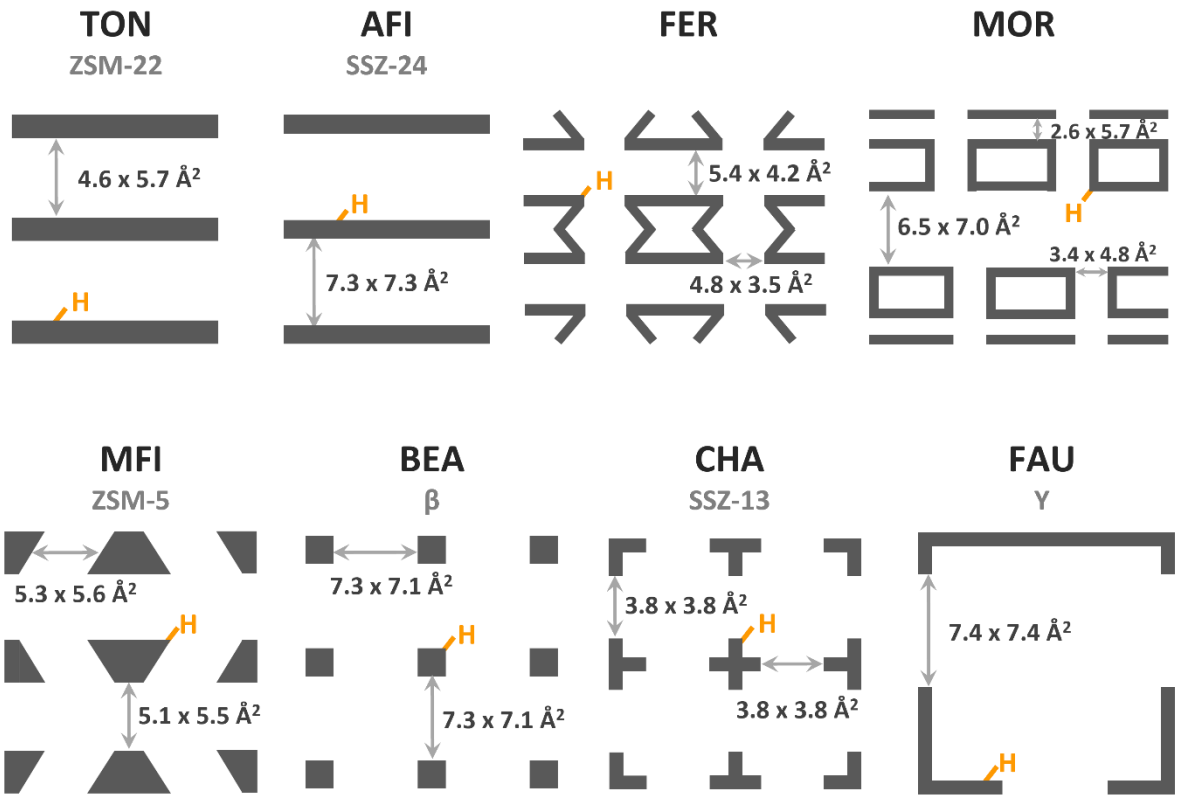

Figure S1. Schematic representation of the investigated zeolite topologies. The dimensions of the channels or cages are taken from the zeolite database of the International Zeolite Association (IZA).[1]

Zeolite ZSM-22 (TON topology) consists of a 1D pore network of narrow 10-ring channels. The zeolite is represented by 1x1x3 supercell with a corresponding Si/Al ratio of 71. The Brønsted acid site is positioned at the T1 site, in agreement with previous theoretical studies who showed the acid proton has no preferred location.[2,3]

Zeolite SSZ-24 (AFI topology) also consists of a 1D pore system of large 12-ring channels. A 1x1x2 supercell model is employed with a Si/Al ratio of 47. Due to the high symmetry of the framework topology, all T sites are equivalent.

Zeolite ZSM-5 (MFI topology) exhibits a 3-dimenional pore architecture, which is characterized by medium-sized, perpendicular straight and sinusoidal 10-ring channels. The

orthorhombic 1x1x1 unit cell has a Si/Al ratio of 95. The Brønsted acid site is created at the T12 position, which is situated at the channel intersection, thus allowing maximal available space for the adsorbed guest species.[4]

Ferrierite (FER topology) is a zeolite consisting of straight 10-ring channels and perpendicular 8-ring channels. The orthorhombic 1x1x2 supercell has a Si/Al ratio of 71. The acid site is created at the T2 position, at the intersection of both channels, in agreement with previous studies.[5,6]

The mordenite zeolite (MOR topology) features parallel large 12-ring channels and small 8-ring channels, which are connected via 8-ring side pockets. The orthorhombic 1x1x2 supercell has a Si/Al ratio of 95. Due to the distinctly different channel systems, the local environment of the possible acid site positions may result in differences in adsorption behavior. The T1 and T4 sites are located in the main 12-ring channel, the T3 site at the intersection of the 8-ring channel and the side pocket, while the T2 site is positioned at the intersection of the main channel and the side pocket. The latter has been identified as one of the most stable acid site positions and is therefore chosen in this work, albeit the energy difference between different locations was shown to be very small.[4]

Zeolite β (BEA topology) is a large pore zeolite with a 3-dimensional channel network consisting of straight 12-ring channels in the a and b direction and a slightly smaller sinusoidal 12-ring channel in the c direction. We employed the polymorph A of zeolite Beta with tetragonal symmetry. The unit cell has a Si/Al ratio of 63 and the acid site is created at the T6 site, providing maximal available space at the intersection of the channels. This acid site has also been employed in multiple previous DFT studies.[7,8] The acid proton is added at the O_{16} position.

Zeolite Y (FAU topology) has a 3-dimensional pore network which consists of large supercages, interconnected by four large 12-ring windows per cage. The 1x1x1 unit cell corresponds to a Si/Al ratio of 47 and all T sites are geometrically equivalent. The acid proton is added at the preferential O_1 position.[4,9]

Zeolite SSZ-13 (CHA topology) is characterized by large elliptic cages which are connected via six small 8-ring windows in each cage. The 1x1x1 unit cell has a Si/Al ratio of 35 and exhibits only equivalent T atoms.

To assess the influence of acid site strength, a number of metal substituted alumino-phosphate zeotypes of the AFI topology (AlPO-5) are considered. Bronsted acid sites are created through isomorphic substitution of either an Al atom by Mg, Sr, Zn, Co and Ni (oxidation state +II) or a P atom by Si, Ge, Ti, Zr and Mn (oxidation state +IV). This results in a set of isostructural frameworks with varying Brønsted acid site strength. Similar to SSZ-24, a 1x1x2 super cell is employed.

***Table S1*.** Summary of the pore architecture, acid site density, acid site position, maximum diameter of a sphere that can be included in the channels/cages and approximate dimensions of the channels or cage windows of the investigated topologies according to the zeolite database of the International Zeolite Association (IZA).[1]

	Pore architecture	**Si/Al ratio**	**Acid site position**	**d_{max}[1] [Å]**	**Dimension[1] [Å²]**
1D zeolites					
TON	straight 10-ring channel	71	T_1O_1	5.7	4.6 x 5.7
AFI	straight 12-ring channel	47	T_1O_2	8.3	7.3 x 7.3
IFR	straight 12-ring channel	63	T_1O_8	7.24	6.2 x 7.2
DON	straight 14-ring channel	127	T_2O_{10}	8.79	8.1 x 8.2
2D zeolites					
MOR	straight 12-ring + 8-ring channel	95	T_1O_1 T_2O_5	6.7	6.5 x 7.0 2.6 x 5.7
FER	straight 10-ring + 8-ring channel	71	T_2O_7	6.3	5.4 x 4.2 4.8 x 3.5
3D zeolites					
MFI	straight + sinusoidal 10-ring channels	95	$T_{12}O_8$	6.3	5.1 x 5.5 5.3 x 5.6
BEA	straight + sinusoidal 12-ring channels	63	T_6O_{16}	6.7	7.3 x 7.1 5.6 x 5.6
FAU	spherical cage with 12-ring windows	47	T_1O_1	11.3	7.4 x 7.4
CHA	elliptical cage with 8-ring windows	35	T_1O_3	7.4	3.8 x 3.8

The equilibrium cell volume and corresponding cell parameters for the static calculations are extracted from a Birch-Murnaghan equation of state fit of energy versus volume.[10] **Table S2** summarizes the unit cell dimensions of the investigated topologies. Note that the influence of the varying acid site density on the adsorption characteristics is assumed to be negligible. This hypothesis seems justified since the Si/Al ratio is quite high and the simulation cells are sufficiently large for all zeolites to minimize the interaction of the guest species with periodic images. Denayer et al. showed that the effect of a varying acid site density on the adsorption enthalpies of alkanes in ZSM-5 and zeolite Y is rather limited for a Si/Al ratio lower than 100.[11,12] Also, Mlinar et al. found the propene oligomerization rate in ZSM-5 to be independent of the acid site density for Si/Al ratios higher than 40.[13]

***Table S2*.** Cell parameters of the different zeolite topologies from the static DFT calculations.

STATIC	a [Å]	b [Å]	c [Å]	α [°]	β [°]	γ [°]
H-ZSM-22	14.03	17.44	14.97	89.27	89.96	89.64
H-SSZ-24	13.86	13.82	16.84	90.02	89.97	120.69
H-SAPO-5	13.92	13.96	17.03	90.05	90.03	119.49
H-FER	19.12	14.32	15.13	90.00	90.00	90.00
H-MOR	18.29	20.29	14.97	89.96	90.09	90.14
H-ZSM-5	20.02	20.25	13.49	89.87	89.69	90.10
H-β	12.69	12.67	26.63	90.00	89.98	90.00
H-Y	17.37	17.34	17.39	59.95	59.88	59.88
H-SSZ-13	13.79	13.78	14.81	90.06	89.99	120.03

The zeolite cell dimensions for the MD simulations are calibrated by performing a preliminary 10 ps ab initio molecular dynamics run in the NpT ensemble at 323 K or 773 K and 1 bar. The unit cell parameters are determined as the time averaged cell parameters from this NpT simulation and are subsequently used for the MD production runs in the NVT ensemble. The equilibration procedure is performed on simulation cells with a single acid site and isobutene adsorbed at the acid site. The obtained cell parameters at 323 K and 773 K are reported in **Table S3** and **Table S4** respectively.

***Table S3*.** Cell parameters of the different zeolite topologies from MD simulations at 323 K.

MD – 323K	a [Å]	b [Å]	c [Å]	α [°]	β [°]	γ [°]
H-ZSM-22	14.17	17.52	15.04	89.32	89.47	90.16
H-SSZ-24	13.89	13.85	16.74	90.03	89.93	120.42
H-SAPO-5	13.99	14.01	16.92	89.89	89.91	120.12
H-MOR	18.42	20.29	15.03	89.96	90.12	90.18
H-ZSM-5	20.14	20.33	13.56	89.82	89.47	90.15
H-Y	17.56	17.50	17.58	59.77	59.66	59.75
H-SSZ-13	13.88	13.88	14.95	90.02	90.15	120.14

***Table S4*.** Cell parameters of the different zeolite topologies from MD simulations at 773 K.

MD – 773K	a [Å]	b [Å]	c [Å]	α [°]	β [°]	γ [°]
H-ZSM-22	14.16	17.62	15.15	89.24	90.56	90.01
H-ITQ-4	19.08	13.78	15.47	91.51	101.42	90.20
H-SSZ-24	13.91	13.87	16.83	90.01	90.05	120.28
H-SAPO-5	14.04	14.07	17.01	89.97	89.85	120.17
H-DON	19.46	23.62	17.13	89.56	90.01	90.14
H-FER	19.11	14.32	15.12	90.00	90.00	90.00
H-MOR	18.41	20.38	15.15	89.96	90.11	90.20
H-ZSM-5	20.38	20.24	13.61	89.92	90.14	89.99
H-β	12.72	12.64	26.84	90.46	90.29	89.99
H-Y	17.57	17.52	17.60	59.62	59.60	59.75
H-SSZ-13	13.83	13.83	14.95	90.14	89.98	119.95

S2. Computational Details

S2.1. Static DFT Calculations

Static geometry optimizations are conducted with the Vienna Ab Initio Simulation package (VASP 5.4),[14–17] using the Projector Augmented Wave (PAW) method[18,19] and the PBE functional[20] as level of theory. Dispersion corrections are added by the Grimme D3 formalism.[21] A plane wave basis set with kinetic energy cutoff of 600 eV and the recommended GW PAW potentials are used.[22] Sampling of the Brillouin zone is restricted to the Γ-point only. The ionic and electronic convergence criteria are set at 10-4 eV and 10-5 eV respectively for all relaxations. The local minima of the adsorption states are optimized with the conjugate gradient algorithm. The cell shape and volume are kept fixed during the optimization. A normal mode analysis is carried out to verify the true nature of the stationary states. The vibrational modes are obtained by applying a partial Hessian vibrational analysis (PHVA)[23–25] on the adsorbate and an 8T cluster of the zeolite framework, centered around the acid site. Thermal corrections and thermodynamic quantities at finite temperature are estimated based on the harmonic oscillator (HO) approximation using the in-house developed TAMkin package.[26]

S2.2. Ab Initio Molecular Dynamics Simulations

Ab initio molecular dynamics (MD) simulations have been performed with the CP2K software package.[27] All simulations employ the revPBE functional[20,28] with additional Grimme D3 dispersion corrections.[21] To approximate the interaction of valence electrons with the atomic cores, GTH pseudopotentials are applied.[29,30] A combination of a double zeta valence polarized (DZVP) Gaussian functions and plane wave functions with an energy cutoff of 320 Ry (GPW)[31,32] are used as basis set.[33] The self-consistent field convergence criterion was set at 10^{-6} Ha. The MD simulations are carried out in the canonical ensemble at a temperature of 323 K or 773 K, which is controlled by a chain of 5 Nosé-Hoover thermostats.[34,35] The system is equilibrated for 5 ps, before starting a production run of 100 ps with a time step of 0.5 fs for integrating the Newtonian equations of motion.

In the course of the simulations, transitions between the different alkene intermediates may occur. To distinguish the different alkene intermediates, an empirical distance criterion was established.[36] The guest hydrocarbon is classified as a physisorbed alkene π-complex if both distances between the acid proton and double bond C atoms are smaller than 2.85 Å; if not a van der Waals complex is sampled. If all distances between a hydrogen atom and a framework oxygen of the acid site, O_z, are larger than 1.25 Å, the intermediate is considered to be a carbenium ion. Finally, an alkoxide is sampled if a covalent C-O_z bond, smaller than 1.9 Å with the framework exists.

S2.3. Umbrella Sampling Simulations

Umbrella sampling (US) simulations[37,38] are carried out to quantify the free energy profiles for isobutene protonation reactions. Within the US technique, the reaction coordinate or collective variable (CV) is divided into a number of equidistant windows, for which individual MD simulations are carried out in parallel to ensure that each point along the reaction coordinate is sampled equally well. A harmonic bias potential, centered around the equilibrium value CV_0 and with bias strength κ, is employed to restrict the sampling to a specific window along the reaction coordinate only.

$$U_b(CV) = \frac{\kappa}{2}(CV - CV_0)^2$$

The CV is defined based on a coordination number (CN) which runs over 2 sets of atoms, i and j, with r_{ij} the interatomic distance and r_0 a reference distance which was set at 1.25Å.

$$CN = \sum_{i,j} \frac{1 - (r_{ij}/r_0)^6}{1 - (r_{ij}/r_0)^{12}}$$

To describe the protonation of the alkene, a single CV is chosen as the CN between the oxygen atoms of the acid site (O_Z) and all hydrogen atoms of the alkene, including the acid proton (H_h), i.e., CN(O_Z – H_h), shown in **Figure S2**. The predefined CV ranges between 0 and 1 and is divided into 38 equidistant windows for which a harmonic bias potential, centered around the CV values of {0.025, 0.05, 0.075, …, 0.925, 0.95}, is applied to restrict the sampling to each window individually. The harmonic constant of the bias potential is 6000 kJ/mol for the windows centered at {0.05, 0.10, 0.15, …, 0.95} or 3000 kJ/mol for the windows centered at {0.075, 0.125, 0.175, …, 0.925} and a total simulation of 30 ps per window is achieved. All umbrella sampling simulations have been performed with the CP2K software package combined with the PLUMED module.[27,39] Simulations are carried out at the revPBE-D3 level of theory[20,21,28] with a triple zeta valence polarized (TZVP) basis set for improved accuracy of the host-guest interactions.[33] All other settings are identical to the regular MD simulations.

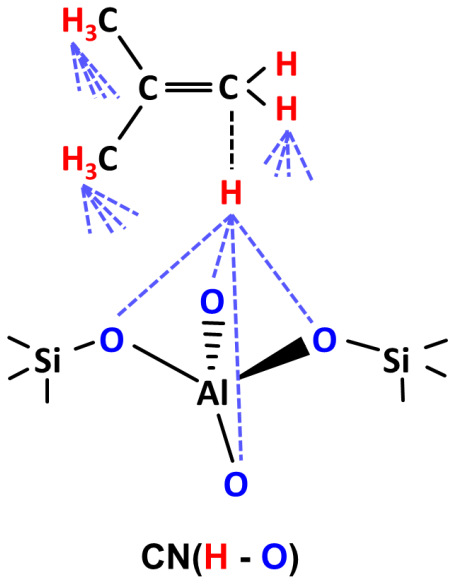

Figure S2. Collective variable describing the protonation of isobutene.

The free energy profile for isobutene protonation is reconstructed by combining the sampling distributions of all windows via the weighted histogram analysis method (WHAM) as implemented in the in-house developed **ThermoLib** software.[40] Kinetic constants are estimated using the expressions from classical transition state theory. Phenomenological free energy barriers, which are independent of the choice of collective variable and take into account the particular shape of the free energy valleys, are calculated according to the procedure described by Bučko et al.[41] and Bailleul et al.[42] A 2-sigma error bar, corresponding to a 95% confidence interval, is computed for the free energy profile obtained from the WHAM analysis using the maximum likelihood estimate (MLE) method as implemented in Thermolib.[42–44] By combining the intrinsic protonation barriers with the statically determined adsorption free energies of isobutene, a rough estimate of the apparent protonation barriers is obtained.

S3. Static Calculations: Thermodynamics

Static calculations are performed at the PBE-D3 level of theory to determine the influence of the zeolite topology and acid site strength on the adsorption characteristics of 2-butene and isobutene intermediates, i.e., physisorbed π-complexes, chemisorbed alkoxides or chemisorbed carbenium ions. Furthermore, to establish linear correlations in order to predict isobutene adsorption energies and protonation barriers, descriptors need to be defined. The dispersion energy contribution of the static isobutene adsorption energy is chosen as descriptor for the zeolite topology, while the static electronic energy for ammonia adsorption is selected as descriptor for the Brønsted acid site strength. **Table S5** contains an overview of the calculated electronic adsorption energies in the different zeolite topologies. **Table S6** contains an overview of the calculated electronic adsorption energies in the metal substituted AlPO-5 materials with varying Brønsted acid site strength. The adsorption enthalpies, entropies and free energies at 323 K and 773 K for all intermediates and materials are listed in **Table S7** through **Table S18**. The optimized geometries of each isobutene intermediate configuration are shown in **Figure S3** through **Figure S6**.

***Table S5*.** Electronic adsorption energies [kJ.mol^{-1}] of the 2-butene and isobutene intermediates in the different zeolite topologies with reference to the empty framework and the alkene in gas phase.

	2-butene π-complex	**2-butoxide**	**isobutene π-complex**	**isobutoxide**	**tert-butoxide**	**tert-butyl cation**
ZSM-22	-115	-110	-112	-101	-77	-91
SSZ-24	-96	-97	-94	-95	-78	-66
ZSM-5	-109	-111	-101	-96	-81	-80
FER	-	-	-96	-92	-57	-72
MOR (T1)	-96	-86	-88	-83	-44	-49
MOR (T2)	-87	-85	-92	-81	-73	-72
β	-	-	-87	-53	-31	-61
SSZ-13	-78	-68	-97	-79	-57	-67
Y	-80	-76	-79	-75	-54	-46

***Table S6*.** Electronic adsorption energies [kJ.mol^{-1}] of ammonia, the 2-butene and isobutene intermediates in the different metal substituted Me-AlPO-5 materials with reference to the empty framework and the alkene in gas phase.

Me-AlPO-5	**NH_3**	**2-butene π-complex**	**2-butoxide**	**isobutene π-complex**	**iso-butoxide**	**tert-butoxide**	**tert-butyl cation**
Mg	-170	-99	-103	-98	-99	-84	-83
Zn	-158	-94	-99	-96	-96	-79	-75
Co	-152	-93	-98	-94	-95	-80	-72
Ni	-146	-94	-97	-94	-94	-80	-66
Sr	-139	-	-	-94	-95	-78	-56
Si	-135	-91	-93	-93	-93	-76	-55
Ge	-127	-90	-94	-90	-91	-74	X
Ti	-119	-88	-94	-89	-91	-73	X
Zr	-117	-87	-93	-91	-90	-73	X
Mn	-86	-84	-87	-85	-87	-70	X

***Table S7*.** Adsorption enthalpies at 323 K [kJ.mol^{-1}] of the 2-butene and isobutene intermediates in the different zeolite topologies with reference to the empty framework and the alkene in gas phase.

	2-butene π-complex	**2-butoxide**	**isobutene π-complex**	**isobutoxide**	**tert-butoxide**	**tert-butyl cation**
ZSM-22	-106	-92	-105	-85	-64	-89
SSZ-24	-90	-83	-93	-82	-69	-56
ZSM-5	-90	-82	-97	-83	-72	-82
FER	-	-	-87	-75	-44	-68
MOR (T1)	-91	-74	-83	-70	-34	-50
MOR (T2)	-82	-73	-89	-69	-64	-73
β	-	-	-82	-40	-21	-62
SSZ-13	-70	-53	-91	-64	-46	-66
Y	-73	-61	-74	-60	-43	-47

***Table S8*.** Adsorption entropies at 323 K [kJ.mol^{-1}] of the 2-butene and isobutene intermediates in the different zeolite topologies with reference to the empty framework and the alkene in gas phase.

	2-butene π-complex	**2-butoxide**	**isobutene π-complex**	**isobutoxide**	**tert-butoxide**	**tert-butyl cation**
ZSM-22	54	63	49	61	66	49
SSZ-24	47	60	50	53	56	49
ZSM-5	58	66	55	64	67	57
FER	-	-	56	63	69	46
MOR (T1)	53	64	54	65	67	47
MOR (T2)	45	60	50	61	66	52
β	-	-	50	61	66	52
SSZ-13	57	62	51	61	67	49
Y	55	63	53	60	66	53

***Table S9*.** Adsorption free energies at 323 K [kJ.mol^{-1}] of the 2-butene and isobutene intermediates in the different zeolite topologies with reference to the empty framework and the alkene in gas phase.

	2-butene π-complex	**2-butoxide**	**isobutene π-complex**	**isobutoxide**	**tert-butoxide**	**tert-butyl cation**
ZSM-22	-52	-29	-56	-24	2	-40
SSZ-24	-43	-23	-43	-29	-13	-7
ZSM-5	-32	-16	-42	-19	-5	-25
FER	-	-	-31	-12	25	-22
MOR (T1)	-38	-10	-29	-5	33	-3
MOR (T2)	-37	-13	-39	-8	2	-21
β	-	-	-32	20	45	-10
SSZ-13	-13	9	-40	-3	21	-17
Y	-18	2	-21	0	23	6

Table S10. Adsorption enthalpies at 773 K [kJ.mol^{-1}] of the 2-butene and isobutene intermediates in the different zeolite topologies with reference to the empty framework and the alkene in gas phase.

	2-butene π-complex	2-butoxide	isobutene π-complex	isobutoxide	tert-butoxide	tert-butyl cation
ZSM-22	-102	-90	-101	-84	-61	-84
SSZ-24	-85	-80	-87	-79	-63	-49
ZSM-5	-85	-79	-91	-81	-67	-75
FER	-	-	-82	-74	-40	-63
MOR (T1)	-86	-71	-78	-68	-30	-43
MOR (T2)	-76	-70	-83	-66	-59	-66
β	-	-	-76	-37	-16	-56
SSZ-13	-65	-50	-86	-62	-42	-60
Y	-68	-58	-69	-58	-39	-41

Table S11. Adsorption entropies at 773 K [kJ.mol^{-1}] of the 2-butene and isobutene intermediates in the different zeolite topologies with reference to the empty framework and the alkene in gas phase.

	2-butene π-complex	2-butoxide	isobutene π-complex	isobutoxide	tert-butoxide	tert-butyl cation
ZSM-22	123	149	111	145	154	110
SSZ-24	106	141	111	123	125	106
ZSM-5	132	155	123	151	153	125
FER	-	-	121	155	164	116
MOR (T1)	120	150	123	152	155	103
MOR (T2)	99	139	110	141	150	114
β	-	-	111	139	150	116
SSZ-13	130	145	115	144	155	110
Y	125	146	120	140	152	119

Table S12. Adsorption free energies at 773 K [kJ.mol^{-1}] of the 2-butene and isobutene intermediates in the different zeolite topologies with reference to the empty framework and alkene in gas phase.

	2-butene π-complex	2-butoxide	isobutene π-complex	isobutoxide	tert-butoxide	tert-butyl cation
ZSM-22	21	59	10	61	93	26
SSZ-24	21	61	24	44	62	57
ZSM-5	47	76	32	70	86	50
FER	-	-	39	81	124	53
MOR (T1)	34	79	45	84	125	60
MOR (T2)	23	69	27	75	91	48
β	-	-	35	102	134	60
SSZ-13	65	95	29	82	113	50
Y	57	88	51	82	113	78

***Table S13*.** Adsorption enthalpies at 323 K [kJ.mol^{-1}] of ammonia, the 2-butene and isobutene intermediates in the different metal substituted Me-AlPO-5 materials with reference to the empty framework and the alkene in gas phase.

Me-AlPO-5	NH_3	2-butene π-complex	2-butoxide	isobutene π-complex	iso-butoxide	tert-butoxide	tert-butyl cation
Mg	-156	-93	-89	-94	-86	-74	-84
Zn	-144	-88	-85	-91	-83	-68	-75
Co	-138	-87	-84	-89	-81	-69	-73
Ni	-133	-88	-79	-89	-80	-68	-68
Sr	-128	-	-	-88	-80	-67	-58
Si	-123	-85	-79	-88	-80	-66	-56
Ge	-115	-83	-80	-85	-84	-63	X
Ti	-107	-76	-80	-84	-73	-62	X
Zr	-104	-75	-79	-80	-72	-63	X
Mn	-76	-77	-74	-78	-73	-59	X

***Table S14*.** Adsorption entropies at 323 K [kJ.mol^{-1}] of ammonia, the 2-butene and isobutene intermediates in the different metal substituted Me-AlPO-5 materials with reference to the empty framework and the alkene in gas phase.

Me-AlPO-5	NH_3	2-butene π-complex	2-butoxide	isobutene π-complex	iso-butoxide	tert-butoxide	tert-butyl cation
Mg	52	52	61	54	61	65	46
Zn	51	54	64	52	63	66	52
Co	51	52	61	53	62	64	46
Ni	54	51	76	46	60	62	47
Sr	51	-	-	48	57	64	53
Si	52	52	64	53	61	64	52
Ge	51	52	62	52	62	64	X
Ti	54	67	61	52	79	66	X
Zr	53	69	63	67	77	64	X
Mn	46	52	67	50	61	66	X

***Table S15*.** Adsorption free energies at 323 K [kJ.mol^{-1}] of ammonia, the 2-butene and isobutene intermediates in the different metal substituted Me-AlPO-5 materials with reference to the empty framework and the alkene in gas phase.

Me-AlPO-5	NH_3	2-butene π-complex	2-butoxide	isobutene π-complex	iso-butoxide	tert-butoxide	tert-butyl cation
Mg	-104	-41	-28	-40	-25	-9	-38
Zn	-93	-34	-21	-39	-20	-2	-23
Co	-87	-35	-23	-36	-19	-5	-27
Ni	-79	-37	-3	-43	-20	-6	-21
Sr	-77	-	-	-40	-23	-3	-5
Si	-71	-33	-15	-35	-19	-2	-4
Ge	-64	-31	-18	-33	-22	1	X
Ti	-53	-9	-19	-32	6	4	X
Zr	-51	-6	-15	-13	5	1	X
Mn	-30	-25	-7	-28	-12	7	X

***Table S16*.** Adsorption enthalpies at 773 K [kJ.mol^{-1}] of ammonia, the 2-butene and isobutene intermediates in the different metal substituted Me-AlPO-5 materials with reference to the empty framework and the alkene in gas phase.

Me-AlPO-5	NH_3	2-butene π-complex	2-butoxide	isobutene π-complex	iso-butoxide	tert-butoxide	tert-butyl cation
Mg	-154	-88	-87	-89	-84	-70	-77
Zn	-141	-83	-82	-86	-81	-64	-69
Co	-136	-81	-81	-84	-79	-65	-66
Ni	-131	-82	-80	-83	-78	-64	-61
Sr	-126	-	-	-81	-77	-63	-51
Si	-121	-80	-76	-82	-78	-62	-50
Ge	-113	-78	-78	-79	-82	-59	X
Ti	-105	-74	-78	-78	-74	-58	X
Zr	-102	-73	-77	-77	-73	-59	X
Mn	-72	-72	-71	-73	-72	-56	X

Table S17. Adsorption entropies at 773 K [kJ.mol^{-1}] of ammonia, the 2-butene and isobutene intermediates in the different metal substituted Me-AlPO-5 materials with reference to the empty framework and the alkene in gas phase.

Me-AlPO-5	NH_3	2-butene π-complex	2-butoxide	isobutene π-complex	iso-butoxide	tert-butoxide	tert-butyl cation
Mg	121	117	142	121	144	150	100
Zn	120	122	149	117	148	153	115
Co	120	116	143	119	146	148	100
Ni	128	112	184	102	142	144	103
Sr	119	-	-	106	132	147	117
Si	122	116	150	119	144	148	117
Ge	120	117	146	117	147	148	X
Ti	127	158	143	116	191	152	X
Zr	126	163	149	157	186	149	X
Mn	106	116	157	112	145	155	X

Table S18. Adsorption free energies at 773 K [kJ.mol^{-1}] of ammonia, the 2-butene and isobutene intermediates in the different metal substituted Me-AlPO-5 materials with reference to the empty framework and the alkene in gas phase.

Me-AlPO-5	NH_3	2-butene π-complex	2-butoxide	isobutene π-complex	iso-butoxide	tert-butoxide	tert-butyl cation
Mg	-33	29	55	32	60	80	23
Zn	-21	39	67	31	67	89	46
Co	-16	35	62	35	67	83	34
Ni	-3	30	104	19	64	80	42
Sr	-7	-	-	25	55	83	66
Si	1	36	74	37	66	86	67
Ge	7	39	68	38	65	89	X
Ti	22	84	65	38	117	94	X
Zr	24	90	72	80	113	90	X
Mn	34	44	86	39	73	99	X

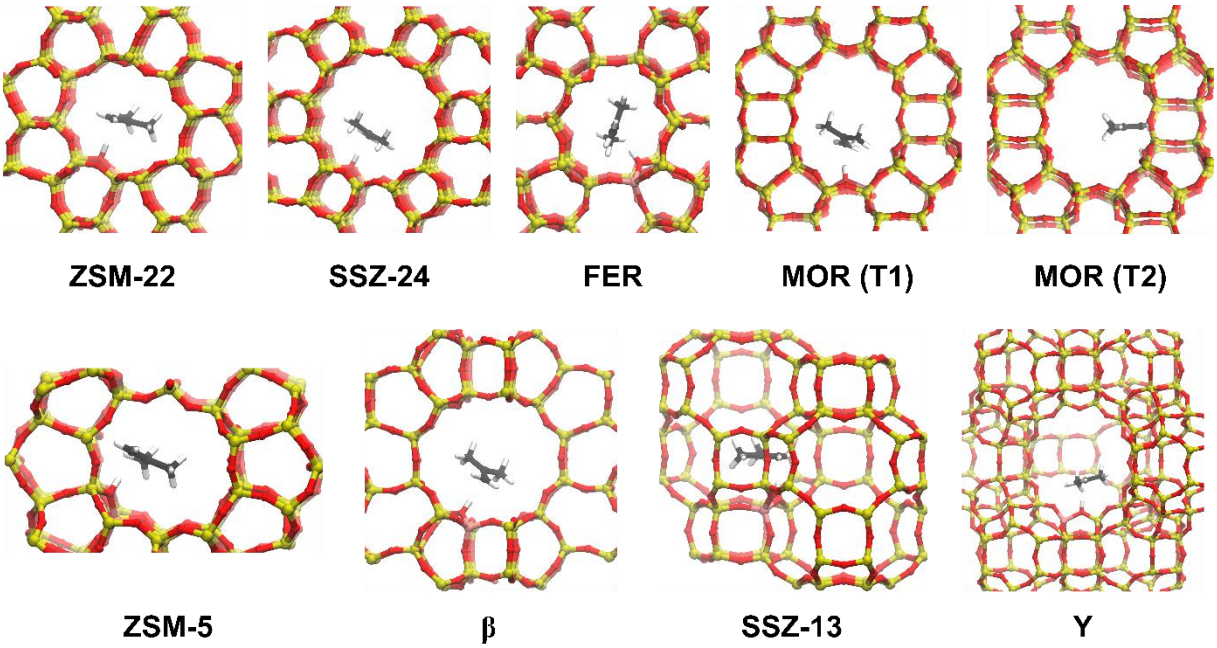

Figure S3. Optimized static geometries (LOT: PBE-D3) of the isobutene π-complex intermediate in the different framework topologies.

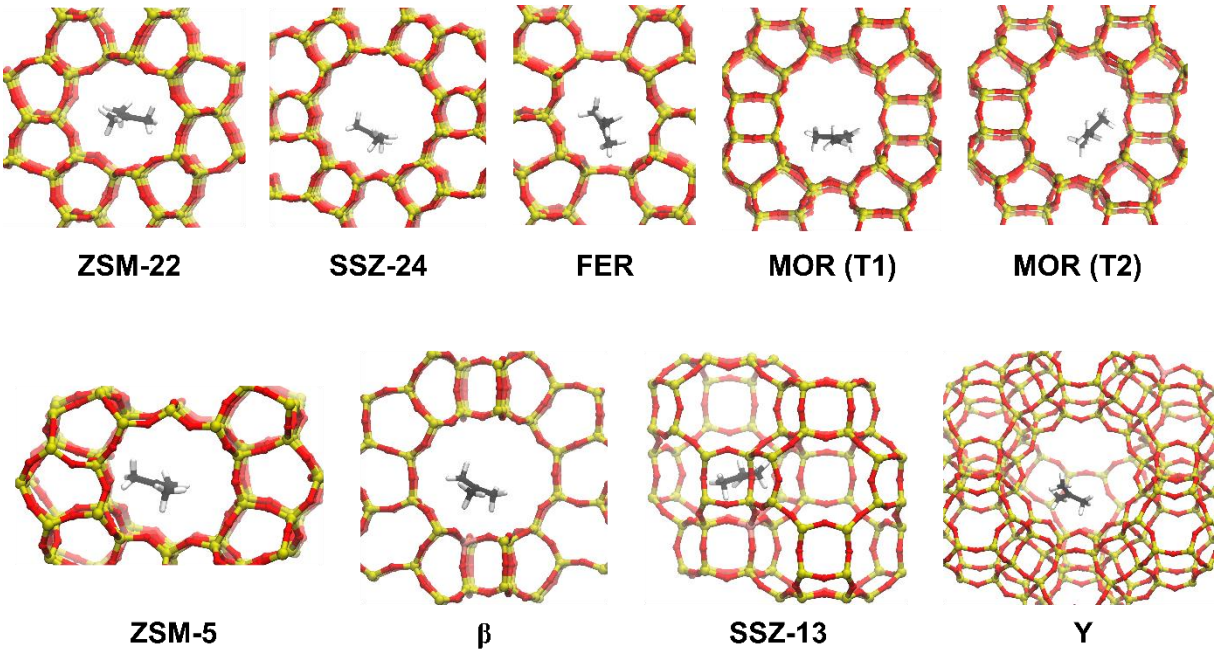

Figure S4. Optimized static geometries (LOT: PBE-D3) of the tert-butyl carbenium ion intermediate in the different framework topologies.

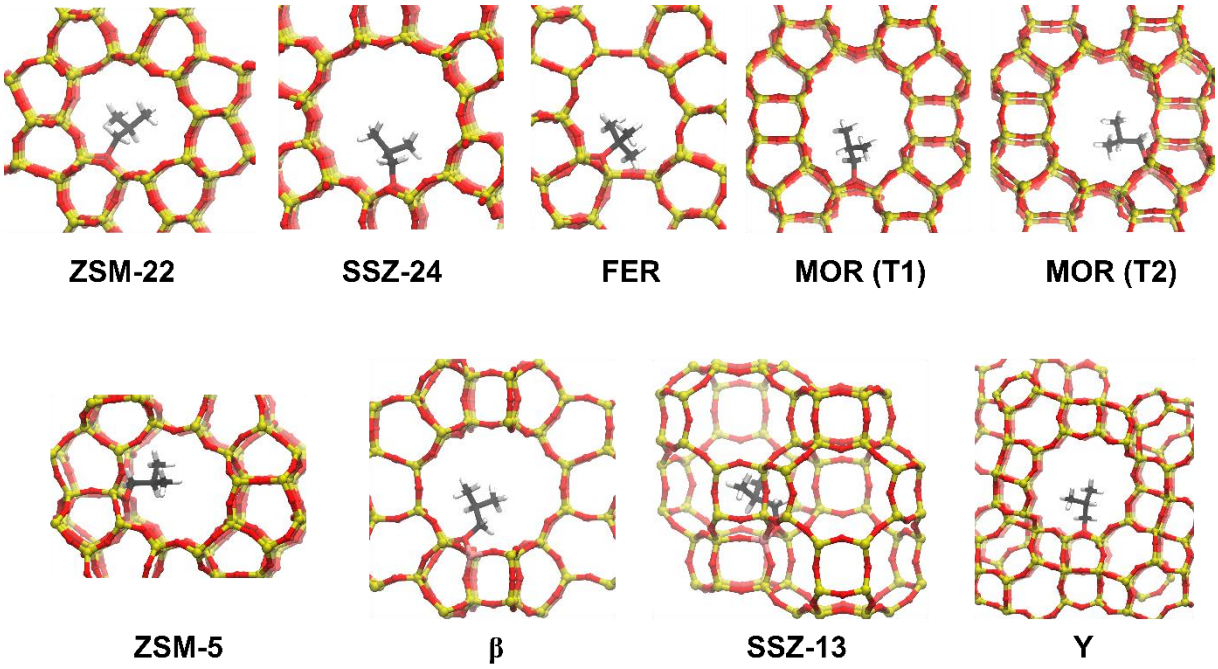

Figure S5. Optimized static geometries (LOT: PBE-D3) of the isobutoxide intermediate in the different framework topologies.

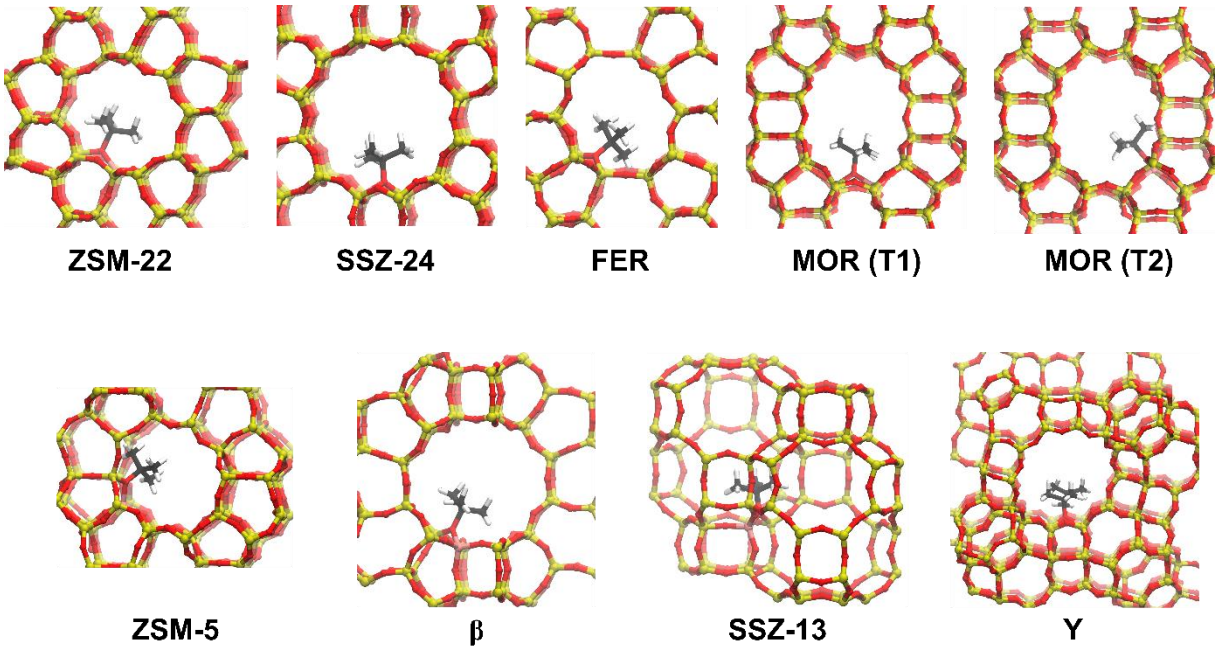

Figure S6. Optimized static geometries (LOT: PBE-D3) of the tert-butoxide intermediate in the different framework topologies.

S4. Regular MD Simulations: Sampling time

Regular MD simulations of the 2-butene and isobutene intermediates in all materials are performed to qualitatively assess the stability of the different physisorbed/chemisorbed species and the influence of the framework environment and acidity on their stability. Simulations are performed at both 323 K and 773 K to highlight the importance of entropy on the stability of the intermediates and a total simulation length of 100 ps for each simulation is ensured to obtain statistically relevant information. Note that even longer simulation lengths would be required to approach a proper ergodic sampling.

In the course of a simulation, transitions between the different alkene intermediates may take place. Therefore, the sampling fraction of each intermediate during a simulation is counted. This sampling fraction represents a qualitative measure for the relative stability of the intermediates. If a transition occurred in the equilibration run or the first 5 ps of the production run, it is checked if this transition is a physically realistic event or merely an equilibration effect and the result of the randomly initialized velocities at the beginning of the MD simulation. Therefore, a constrained simulation of 40 ps is performed in which quadratic walls were added to the simulation to prevent transitions between different intermediates. Afterwards, these constraints are lifted and a regular MD production run of 100 ps is performed.

To distinguish the different alkene intermediates, an empirical distance criterion was established.[36,45] The guest hydrocarbon is classified as a physisorbed alkene π-complex if both distances between the acid proton and double bond C atoms are smaller than 2.85 Å; if not a van der Waals complex is sampled. If all distances between a hydrogen atom and a framework oxygen of the acid site, O_z, are larger than 1.25 Å, the intermediate is considered to be a carbenium ion. Finally, an alkoxide is sampled if a covalent C-O_z bond, smaller than 1.9 Å with the framework exists.

For each material, three simulations are carried out for linear butene with either the 2-butene π-complex, 2-butyl carbenium ion or 2-butoxide as initial configurations. For the branched isobutene, four simulations are performed with either the isobutene π-complex, the tert-butyl carbenium ion, the isobutoxide or the tert-butoxide as initial configurations. The resulting sampling percentages of the intermediates during these simulations at 323 K or 773 K are listed in **Table S19** through **Table S22** for all materials. **Figure S7** and **Figure S8** as well as **Figure 4** and **Figure 8** in the main manuscript show the influence of topology and acid strength on the sampling time and hence stability of the 2-butene and isobutene intermediates respectively. Note that the results of the simulations starting from a π-complex configuration and carbenium ion configuration are averaged and displayed in **Figure 4** and **Figure 8**. Averaging the sampling fractions is allowed as due to the regular transitions taking place between the vdW-complex, π-complex and carbenium ion configurations, both simulations actually describe the same ensemble of configurations. Finally, also note that for zeolite MOR, 2 acid site positions were considered, the T1 site located in the main 12-ring

channel and the T2 site located at the intersection of the main channel and the 8-ring side pocket which provides an additional (partial) confinement for the adsorbates.

At low temperature, the 2-butene π-complex and 2-butoxide are stable intermediates in all frameworks. At cracking temperature, both the alkoxide and π-complex suffer from entropic penalties, resulting in the 2-butene vdW-complex becoming the most stable state in all frameworks. The importance of the zeolite pore topology on the stability of the physisorbed linear alkenes and alkoxides is rather subtle.

In the narrow 1D 10-ring channels of ZSM-22, the 2-butene π-complex exists as a very stable intermediate, even with a sampling probability of around 40% at high temperature. On the other hand, in the larger 1D 12-ring channels of SSZ-24, the more freely adsorbed 2-butene vdW-complex is significantly more favored with a sampling probability of more than 90% at 773 K. Remarkably, ZSM-22 is also the only zeolite in which the 2-butyl carbenium ion has a finite lifetime at cracking conditions. Due to the much better confinement, guest species can be more stabilized and hence more strongly adsorbed than in the spacious channels of SSZ-24. Simultaneously, the entropy loss upon formation of a physisorbed π-complex will be much lower in ZSM-22 than in the SSZ-24, thus explaining their higher preference for a 2-butene vdW-complex.

***Table S19*.** Sampling percentages for the MD simulations on the linear butene intermediates at 323K.

ZSM-22	**π-complex**	**vdW complex**	**carbocation**	**alkoxide**
2-butene π-complex	97	3	0	0
2-butyl carbocation	100	0	0	0
2-butoxide	0	0	0	100
SSZ-24	**π-complex**	**vdW complex**	**carbocation**	**alkoxide**
2-butene π-complex	67	33	0	0
2-butyl carbocation	60	40	0	0
2-butoxide	0	0	0	100
ZSM-5	**π-complex**	**vdW complex**	**carbocation**	**alkoxide**
2-butene π-complex	99	1	0	0
2-butyl carbocation	97	3	0	0
2-butoxide	0	0	0	100
MOR (T1)	**π-complex**	**vdW complex**	**carbocation**	**alkoxide**
2-butene π-complex	86	14	0	0
2-butyl carbocation	71	29	0	0
2-butoxide	0	0	0	100
MOR (T2)	**π-complex**	**vdW complex**	**carbocation**	**alkoxide**
2-butene π-complex	54	46	0	0
2-butyl carbocation	53	47	0	0
2-butoxide	0	0	0	100
Y	**π-complex**	**vdW complex**	**carbocation**	**alkoxide**
2-butene π-complex	97	3	0	0
2-butyl carbocation	97	3	0	0
2-butoxide	0	0	0	100
SSZ-13	**π-complex**	**vdW complex**	**carbocation**	**alkoxide**
2-butene π-complex	61	39	0	0
2-butyl carbocation	95	5	0	0
2-butoxide	0	0	0	100
MgAlPO-5	**π-complex**	**vdW complex**	**carbocation**	**alkoxide**
2-butene π-complex	99	1	0	0
2-butyl carbocation	97	3	0	0
2-butoxide	0	0	0	100
SAPO-5	**π-complex**	**vdW complex**	**carbocation**	**alkoxide**
2-butene π-complex	81	19	0	0
2-butyl carbocation	53	47	0	0
2-butoxide	0	0	0	100
ZrAlPO-5	**π-complex**	**vdW complex**	**carbocation**	**alkoxide**
2-butene π-complex	74	26	0	0
2-butyl carbocation	81	19	0	0
2-butoxide	0	0	0	100

***Table S20*.** Sampling percentages for the MD simulations on the linear butene intermediates at 773K. (X denotes that the alkoxide intermediate is unstable and immediately transforms into a carbenium ion/π-complex at the start of the production run)

ZSM-22	**π-complex**	**vdW complex**	**carbocation**	**alkoxide**
2-butene π-complex	41	50	9	0
2-butyl carbocation	67	27	6	0
2-butoxide	X	X	X	X
SSZ-24	**π-complex**	**vdW complex**	**carbocation**	**alkoxide**
2-butene π-complex	4	96	0	0
2-butyl carbocation	4	96	0	0
2-butoxide	X	X	X	X
ZSM-5	**π-complex**	**vdW complex**	**carbocation**	**alkoxide**
2-butene π-complex	32	68	0	0
2-butyl carbocation	32	68	0	0
2-butoxide	X	X	X	X
MOR (T1)	**π-complex**	**vdW complex**	**carbocation**	**alkoxide**
2-butene π-complex	3	97	0	0
2-butyl carbocation	4	92	4	0
2-butoxide	X	X	X	X
MOR (T2)	**π-complex**	**vdW complex**	**carbocation**	**alkoxide**
2-butene π-complex	6	93	1	0
2-butyl carbocation	16	84	0	0
2-butoxide	X	X	X	X
Y	**π-complex**	**vdW complex**	**carbocation**	**alkoxide**
2-butene π-complex	7	93	0	0
2-butyl carbocation	8	92	0	0
2-butoxide	X	X	X	X
SSZ-13	**π-complex**	**vdW complex**	**carbocation**	**alkoxide**
2-butene π-complex	0	100	0	0
2-butyl carbocation	14	86	0	0
2-butoxide	11	74	0	15
MgAlPO-5	**π-complex**	**vdW complex**	**carbocation**	**alkoxide**
2-butene π-complex	4	91	5	0
2-butyl carbocation	8	89	3	0
2-butoxide	X	X	X	X
SAPO-5	**π-complex**	**vdW complex**	**carbocation**	**alkoxide**
2-butene π-complex	5	95	0	0
2-butyl carbocation	6	94	0	0
2-butoxide	2	75	0	23
ZrAlPO-5	**π-complex**	**vdW complex**	**carbocation**	**alkoxide**
2-butene π-complex	5	95	0	0
2-butyl carbocation	2	98	0	0
2-butoxide	4	62	0	34

***Table S21*.** Sampling percentages for the MD simulations on the isobutene intermediates at 323K. (X denotes that the alkoxide intermediate is unstable and immediately transforms into a carbenium ion/π-complex at the start of the production run)

ZSM-22	**π-complex**	**vdW complex**	**carbocation**	**alkoxide**
isobutene π-complex	0	0	100	0
tert-butyl carbocation	2	0	98	0
isobutoxide	0	0	0	100
tert-butoxide	X	X	X	X
SSZ-24	**π-complex**	**vdW complex**	**carbocation**	**alkoxide**
isobutene π-complex	33	17	50	0
tert-butyl carbocation	12	35	53	0
isobutoxide	0	0	0	100
tert-butoxide	X	X	X	X
ZSM-5	**π-complex**	**vdW complex**	**carbocation**	**alkoxide**
isobutene π-complex	45	5	50	0
tert-butyl carbocation	13	1	86	0
isobutoxide	0	0	0	100
tert-butoxide	X	X	X	X
MOR (T1)	**π-complex**	**vdW complex**	**carbocation**	**alkoxide**
isobutene π-complex	20	80	0	0
tert-butyl carbocation	11	41	48	0
isobutoxide	0	0	0	100
tert-butoxide	X	X	X	X
MOR (T2)	**π-complex**	**vdW complex**	**carbocation**	**alkoxide**
isobutene π-complex	54	10	36	0
tert-butyl carbocation	52	3	45	0
isobutoxide	0	0	0	100
tert-butoxide	X	X	X	X
Y	**π-complex**	**vdW complex**	**carbocation**	**alkoxide**
isobutene π-complex	82	3	15	0
tert-butyl carbocation	83	4	13	0
isobutoxide	0	0	0	100
tert-butoxide	X	X	X	X
SSZ-13	**π-complex**	**vdW complex**	**carbocation**	**alkoxide**
isobutene π-complex	26	19	55	0
tert-butyl carbocation	0	0	100	0
isobutoxide	0	0	0	100
tert-butoxide	X	X	X	X
MgAlPO-5	**π-complex**	**vdW complex**	**carbocation**	**alkoxide**
isobutene π-complex	1	0	99	0
tert-butyl carbocation	0	0	100	0
isobutoxide	0	0	0	100
tert-butoxide	X	X	X	X
SAPO-5	**π-complex**	**vdW complex**	**carbocation**	**alkoxide**
isobutene π-complex	85	15	0	0
tert-butyl carbocation	84	16	0	0
isobutoxide	0	0	0	100
tert-butoxide	X	X	X	X
ZrAlPO-5	**π-complex**	**vdW complex**	**carbocation**	**alkoxide**
isobutene π-complex	81	19	0	0
tert-butyl carbocation	85	15	0	0
isobutoxide	0	0	0	100
tert-butoxide	0	0	0	100

Table S22. Sampling percentages for the MD simulations on the isobutene intermediates at 773K. (X denotes that the alkoxide intermediate is unstable and immediately transforms into a carbenium ion/π-complex at the start of the production run)

ZSM-22	**π-complex**	**vdW complex**	**carbocation**	**alkoxide**
isobutene π-complex	1	3	96	0
tert-butyl carbocation	4	1	95	0
isobutoxide	0	0	0	100
tert-butoxide	X	X	X	X
SSZ-24	**π-complex**	**vdW complex**	**carbocation**	**alkoxide**
isobutene π-complex	1	37	62	0
tert-butyl carbocation	2	27	71	0
isobutoxide	0	0	0	100
tert-butoxide	X	X	X	X
ZSM-5	**π-complex**	**vdW complex**	**carbocation**	**alkoxide**
isobutene π-complex	1	11	88	0
tert-butyl carbocation	3	6	91	0
isobutoxide	0	0	0	100
tert-butoxide	X	X	X	X
MOR (T1)	**π-complex**	**vdW complex**	**carbocation**	**alkoxide**
isobutene π-complex	2	98	0	0
tert-butyl carbocation	2	31	67	0
isobutoxide	0	0	0	100
tert-butoxide	X	X	X	X
MOR (T2)	**π-complex**	**vdW complex**	**carbocation**	**alkoxide**
isobutene π-complex	2	45	53	0
tert-butyl carbocation	2	37	61	0
isobutoxide	0	0	0	100
tert-butoxide	X	X	X	X
Y	**π-complex**	**vdW complex**	**carbocation**	**alkoxide**
isobutene π-complex	1	99	0	0
tert-butyl carbocation	2	37	61	0
isobutoxide	0	0	0	100
tert-butoxide	X	X	X	X
SSZ-13	**π-complex**	**vdW complex**	**carbocation**	**alkoxide**
isobutene π-complex	1	26	73	0
tert-butyl carbocation	0	2	98	0
isobutoxide	0	0	0	100
tert-butoxide	X	X	X	X
MgAlPO-5	**π-complex**	**vdW complex**	**carbocation**	**alkoxide**
isobutene π-complex	0	0	100	0
tert-butyl carbocation	0	0	100	0
isobutoxide	0	0	0	100
tert-butoxide	X	X	X	X
SAPO-5	**π-complex**	**vdW complex**	**carbocation**	**alkoxide**
isobutene π-complex	1	99	0	0
tert-butyl carbocation	3	95	2	0
isobutoxide	0	0	0	100
tert-butoxide	X	X	X	X
ZrAlPO-5	**π-complex**	**vdW complex**	**carbocation**	**alkoxide**
isobutene π-complex	3	97	0	0
tert-butyl carbocation	2	98	0	0
isobutoxide	0	0	0	100
tert-butoxide	X	X	X	X

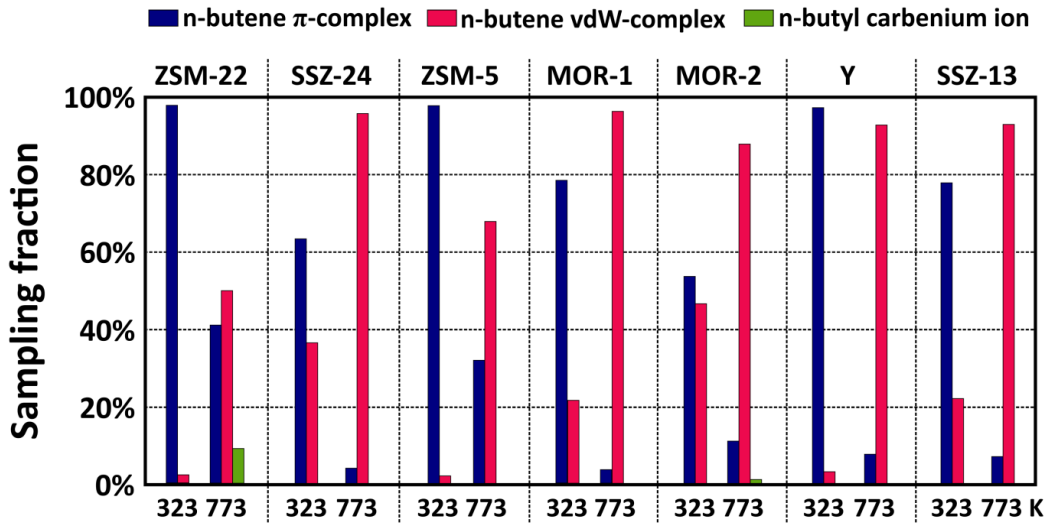

Figure S7. Sampling probability of the π-complex, vdW-complex and carbenium ion intermediates during MD simulations of the linear butene species in different zeolite topologies at 323K and 773K. Results are averaged from 2 independent simulations with either the π-complex and carbenium ion as initial configuration.

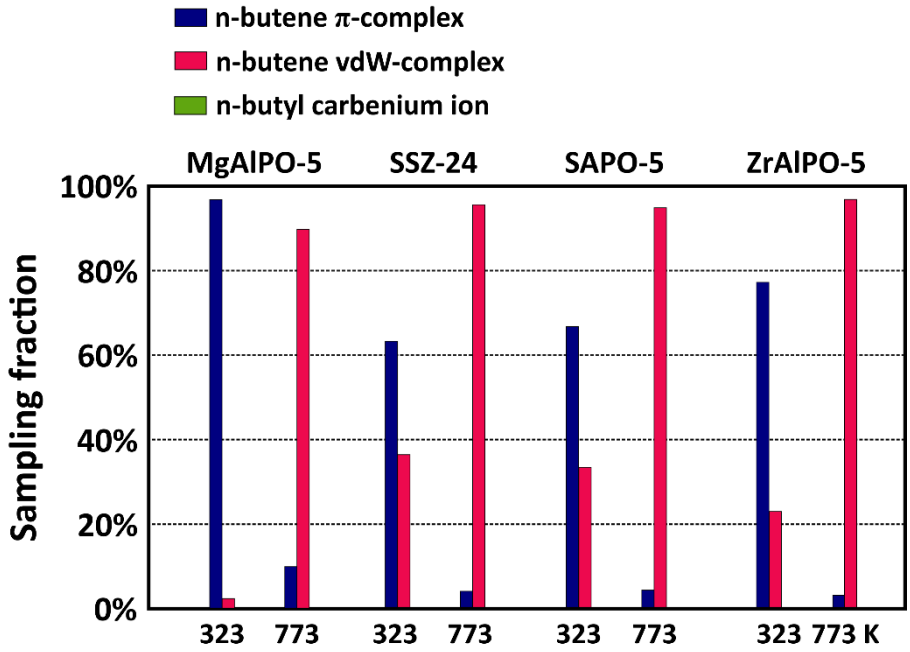

Figure S8. Sampling probability of the π-complex, vdW-complex and carbenium ion intermediates during MD simulations of the linear butene species in the different metal substituted AlPO-5 materials with different acid site strength and H-SSZ-24 at 323K and 773K. Results are averaged from 2 independent simulations with either the π-complex and carbenium ion as initial configuration.

S5. Regular MD Simulations: Mobility

To make a qualitative assessment of the entropy of the adsorbed isobutene intermediates in the different zeolite topologies, the mobility of these species during an MD simulation can be analyzed. Starting from an MD trajectory, we can track the location of the center-of-mass (COM) of the guest molecule inside the pores of the zeolite. This allows to make scatter plots of the COM location and probability distributions along each axis of the coordinate system. Based on these probability distributions, the translational entropy of the species can be computed.

To compute the translational entropy, we start from the expression of the classical partition function in the canonical ensemble:

$$\mathrm{Z} = \frac{1}{\mathrm{h}^{3\mathrm{N}}} \int \mathrm{e}^{-\beta \mathrm{H}(\vec{\mathrm{r}}^{\mathrm{N}}, \vec{\mathrm{p}}^{\mathrm{N}})} \, \mathrm{d}\vec{\mathrm{p}}^{\mathrm{N}} \mathrm{d}\vec{\mathrm{r}}^{\mathrm{N}}$$

The integration over the momenta can be separated and performed analytically, and leads to the translational partition function:

$$\mathrm{Z} = \mathrm{C}_{tr} \int \mathrm{e}^{-\beta \mathrm{V}(\vec{\mathrm{r}}^{\mathrm{N}})} \, \mathrm{d}\vec{\mathrm{r}}^{\mathrm{N}}$$

with

$$\mathrm{C}_{tr} = \frac{1}{\mathrm{h}^{3N}} \left(\frac{2\pi}{\beta} \right)^{\frac{3N}{2}}$$

One can introduce the configurational probability density as:

$$\mathrm{p}(\vec{\mathrm{r}}^{\mathrm{N}}) = \frac{\mathrm{C}_{tr}}{\mathrm{Z}} \mathrm{e}^{-\beta \mathrm{V}(\vec{\mathrm{r}}^{\mathrm{N}})}$$

with the normalization $\int \mathrm{p}(\vec{\mathrm{r}}^{\mathrm{N}}) \mathrm{d}\vec{\mathrm{r}}^{\mathrm{N}} = 1$.

The entropy is defined as:

$$\mathrm{S} = -\left(\frac{\partial \mathrm{F}}{\partial \mathrm{T}} \right)_{\mathrm{N,V}} = \mathrm{k_B} \ln \mathrm{Z} - \mathrm{k_B} \beta \left(\frac{\partial \ln \mathrm{Z}}{\partial \beta} \right)_{\mathrm{N,V}}$$

Using the configurational probability density, we can rewrite the entropy as:

$$\mathrm{S} = \mathrm{k_B} \ln \mathrm{C} - \mathrm{k_B} \beta \frac{\partial}{\partial \beta} ln C_{tr} - \mathrm{k_B} \int \mathrm{p}(\vec{\mathrm{r}}^{\mathrm{N}}) \ln\left(\mathrm{p}(\vec{\mathrm{r}}^{\mathrm{N}}) \right) \mathrm{d}\vec{\mathrm{r}}^{\mathrm{N}}$$

where the first two terms contain the kinetic contribution, while the second term represents the configurational contribution. Furthermore, if we consider an isolated molecule, we can isolate the center-of-mass (COM) translations from the configurational contribution of the entropy. This can be done by expressing that the COM position can be perfectly decoupled from all other internal degrees of freedom:

$$p(\vec{r}^N) = p_R(\vec{R})p_q(\vec{q}^{N-1})$$
$$d\vec{r}^N = J \cdot d\vec{R}d\vec{q}^{N-1}$$

in which $J = \left|\frac{\partial[\vec{r}^N]}{\partial[\vec{R},\vec{q}^{N-1}]}\right|$ represents the Jacobian for the transformation of Cartesian coordinates $\vec{r}^N$ to the COM and internal coordinates $\vec{q}^{N-1}$. Due to the fact that the COM can be perfectly decoupled from the internal coordinates, the Jacobian is unity. As a result, the configurational entropy can be rewritten as:

$$\begin{aligned}
S_{conf} &= -k_B \int p(\vec{r}^N) \ln\left(p(\vec{r}^N)\right) d\vec{r}^N \\
&= -k_B \int p_R(\vec{R})p_q(\vec{q}^{N-1}) \ln\left(p_R(\vec{R})p_q(\vec{q}^{N-1})\right) d\vec{R}d\vec{q}^{N-1} \\
&= -k_B \int p_R(\vec{R}) \ln\left(p_R(\vec{R})\right) d\vec{R} \int p_q(\vec{q}^{N-1}) d\vec{q}^{N-1} \\
&\qquad - k_B \int p_R(\vec{R}) d\vec{R} \int p_q(\vec{q}^{N-1}) \ln\left(p_q(\vec{q}^{N-1})\right) d\vec{q}^{N-1} \\
&= -k_B \int p_R(\vec{R}) \ln\left(p_R(\vec{R})\right) d\vec{R} - k_B \int p_q(\vec{q}^{N-1}) \ln\left(p_q(\vec{q}^{N-1})\right) d\vec{q}^{N-1} \\
&= S_R + S_q
\end{aligned}$$

Where S_R and S_q represent the contributions to the configurational entropy related to the COM translations (i.e. the translational entropy) and the internal degrees of freedom respectively. Furthermore, due to the fact that the X, Y and Z components of the COM are also decoupled from each other, with corresponding probability distributions p_X, p_Y and p_Z, the translational entropy can be further expanded as:

$$\begin{aligned}
S_R &= S_X + S_Y + S_Z \\
&= -k_B \int p_X(X) \ln\left(p_X(X)\right) dX - k_B \int p_Y(Y) \ln\left(p_Y(Y)\right) dY - k_B \int p_Z(Z) \ln\left(p_Z(Z)\right) dZ
\end{aligned}$$

Finally, we will apply this formula to estimate the translational entropy of a guest molecule adsorbed inside the pores of a zeolite. Although the guest COM is not fully decoupled from the zeolite degrees of freedom due to the guest-zeolite interaction, we will assume these interactions be weak enough to still be able to apply the above formula to estimate the translational entropy.

The resulting translational contributions to the entropy, obtained from regular MD simulations at 323 K and 773 K are listed in **Table S23** for the isobutene adsorbates. Note that during most MD simulations, an equilibrium between neutral isobutene and the protonated tert-butyl carbenium ion is sampled. The calculated translational entropy values are therefore also computed for this equilibrium of both states. Also note that the reported values are the average of the translational entropy from two MD simulations, starting either from an isobutene π-complex or a tert-butyl carbenium ion configuration, to obtain a more reliable estimate. The lowest mobility and translational entropy is observed for the narrow pore zeolites ZSM-5 and ZSM-22, where the 10-ring channels provide a strong adsorption and reduced configurational freedom. In the large pore 12-ring channel zeolites SSZ-24 and MOR, the mobility of the physisorbed isobutene intermediates is significantly enhanced and isobutene can quite freely diffuse along the channel direction. Also in the chabazite cages of SSZ-13, the mobility of the isobutene intermediates is rather restricted, which might be caused by the hindered diffusion of isobutene through the small 8-ring windows that connect different cages. On the other hand, the faujasite supercages of zeolite Y result in a free isobutene diffusion and consequently large mobility and translational entropy.

***Table S23*.** Translational entropy for the physisorbed isobutene/ tert-butyl carbenium ion equilibrium in 100 ps regular MD simulations at 323 K and 773K in the different zeolite materials.

Topology	$S_{transl,\ 323K}$ [J.mol^{-1}.K^{-1}]	$S_{transl,\ 773K}$ [J.mol^{-1}.K^{-1}]
ZSM-22	2.41	3.72
SSZ-24	4.96	19.27
ZSM-5	3.31	2.53
MOR (T2)	5.48	21.64
SSZ-13	3.40	3.95
Y	9.58	46.36

To assess the importance of mobility and entropy effects on the protonation of isobutene in the different zeolite topologies, the translational entropy is computed for both the reactant state (physisorbed isobutene) and the protonation transition state from the trajectories of the umbrella sampling simulations. To obtain more reliable estimates, the average translational entropy is computed from six neighboring windows located around the reactant well for the reactant state and from six neighboring windows around the transition state region for the transition state. **Table S24** summarizes the computed translational entropy values for the reactant, transition state as well as the translational entropy barrier for the protonation reaction in the different topologies. Interestingly, for the 10-ring channel zeolite topologies, ZSM-22 and ZSM-5, no increase or decrease in translational entropy occurs upon isobutene protonation. Therefore, both the physisorbed isobutene reactant and

protonation transition state exhibit a similar degree of conformational freedom and the protonation will be almost exclusively governed by enthalpic effects. Also for the cage topology SSZ-13 and the FER topology, a very small decrease in mobility and translational entropy upon formation of the transition state can be distinguished. The medium or large sized pore zeolites with a 12-ring channel system such as ITQ-4, SSZ-24, MOR and β are all characterized by a considerable loss of translational entropy and hence mobility upon protonation of the double bond, varying from -8 to -20 $J.mol^{-1}.K^{-1}$. Therefore, next to the enthalpic effects, the reduced conformational freedom and entropy will contribute to the overall protonation barrier. Finally, in the extra-large pore zeolites such as the 14-ring channel zeolite DON and the supercage topology Y, the protonation of isobutene is accompanied by a high reduction in translational entropy of -33 to -35 $J.mol^{-1}.K^{-1}$. In this case, the reduction in mobility and configurational freedom required to protonate isobutene will result in a substantial contribution to the overall protonation barrier – next to the enthalpic contribution – and might even be responsible for one third up to one half of the total barrier. Since the entropic contribution for the protonation becomes clearly non-negligible in this case, it may explain why an elementary descriptor based mainly on enthalpic effects to distinguish framework topologies might prove ineffective for zeolites consisting of a very large pore system.

Table S24. Translational entropy for the physisorbed isobutene (reactant) and isobutene protonation transition states at 773K in the different zeolite materials.

Topology	$S_{transl,\ rea}$ **[J.mol^{-1}.K^{-1}]**	$S_{transl,\ TS}$ **[J.mol^{-1}.K^{-1}]**	$\Delta S_{transl,\ TS-\ rea}$ **[J.mol^{-1}.K^{-1}]**
ZSM-22	3.47	3.88	0.41
SSZ-24	21.87	4.55	-17.32
ITQ-4	13.47	5.41	-8.06
DON	43.53	10.34	-33.19
ZSM-5	2.81	2.73	-0.08
FER	2.89	1.38	-1.51
MOR	19.87	4.52	-15.35
β	23.58	3.64	-19.94
SSZ-13	3.51	2.59	-0.92
Y	42.57	7.46	-35.11

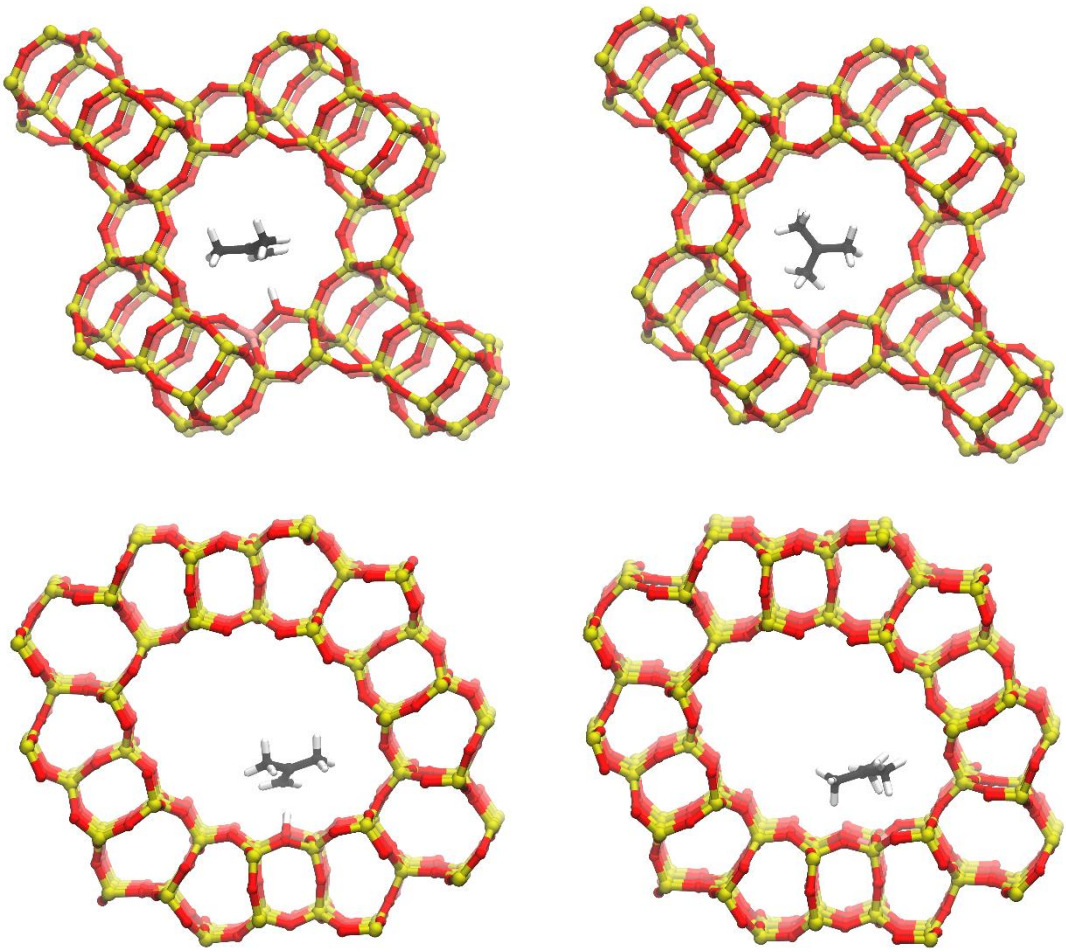

Figure S9. Snapshots of an adsorbed isobutene pi-complex and tert-butyl carbenium ion configuration in zeolite topologies ITQ-4 (top) and DON (bottom) during the US simulations of isobutene protonation at 773 K.

S6. Umbrella Sampling Overview

An overview of the Helmholtz free energy profiles for isobutene protonation in the tert-butyl carbenium ion at 773 K is given in **Figure S10** for the one-dimensional zeolite topologies, **Figure S11** for the multi-dimensional zeolite topologies and **Figure S12** for the metal substituted MeAlPO-5 topologies with varying Brønsted acid strength. For each free energy profile, the error bar corresponding to a 95% confidence interval, obtained from the MLE method is highlighted by the colored area. A summary of the computed phenomenological protonation free energy barriers and reaction free energies (free energy difference between physisorbed isobutene and the tert-butyl carbenium ion) is given in **Table S25**.

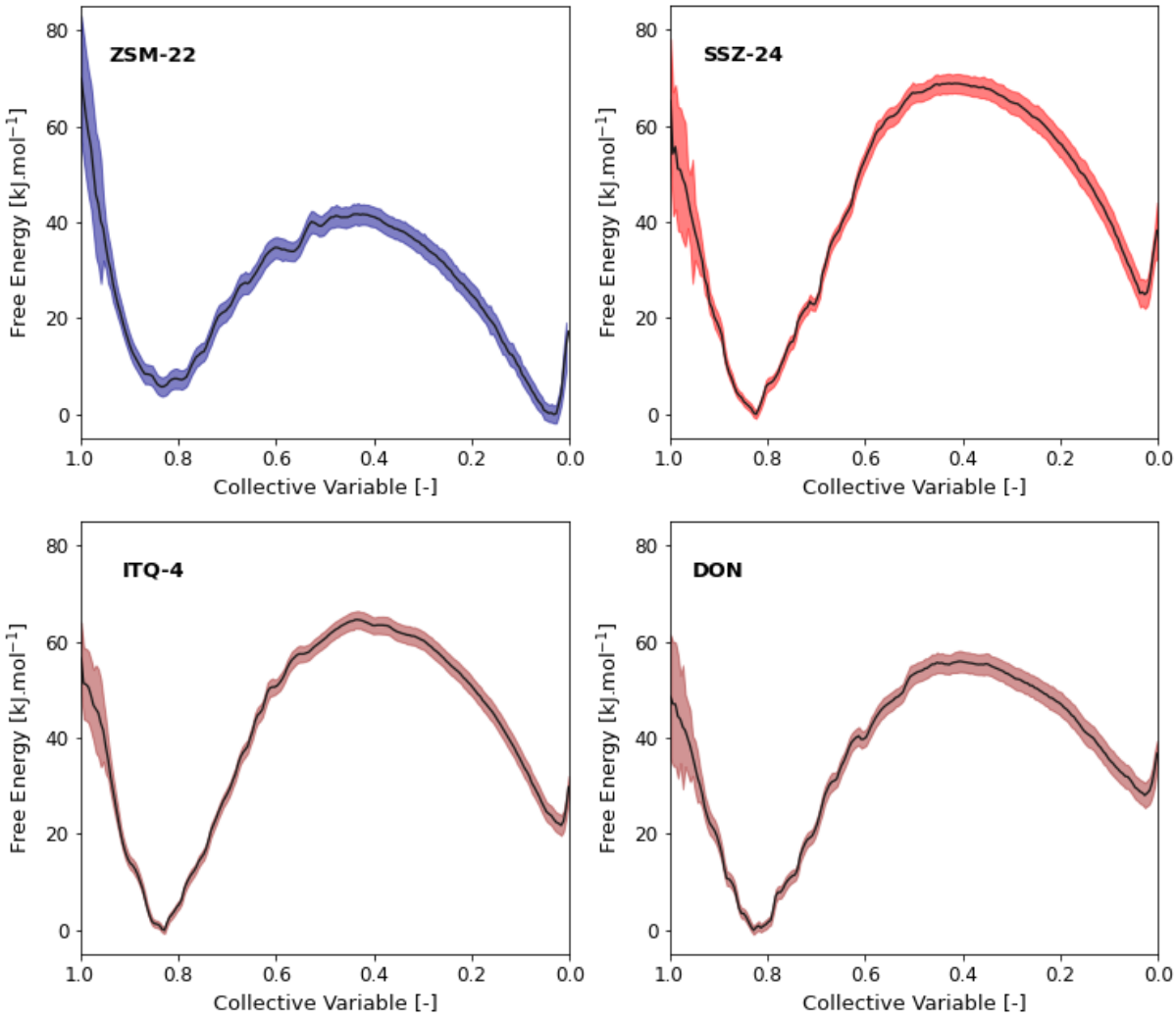

Figure S10. Free energy profiles at 773K for isobutene protonation into a tert-butyl carbenium ion in the one-dimensional zeolite topologies ZSM-22, SSZ-24, ITQ-4 and DON with indication of the error bars (colored area) as obtained from the MLE method.

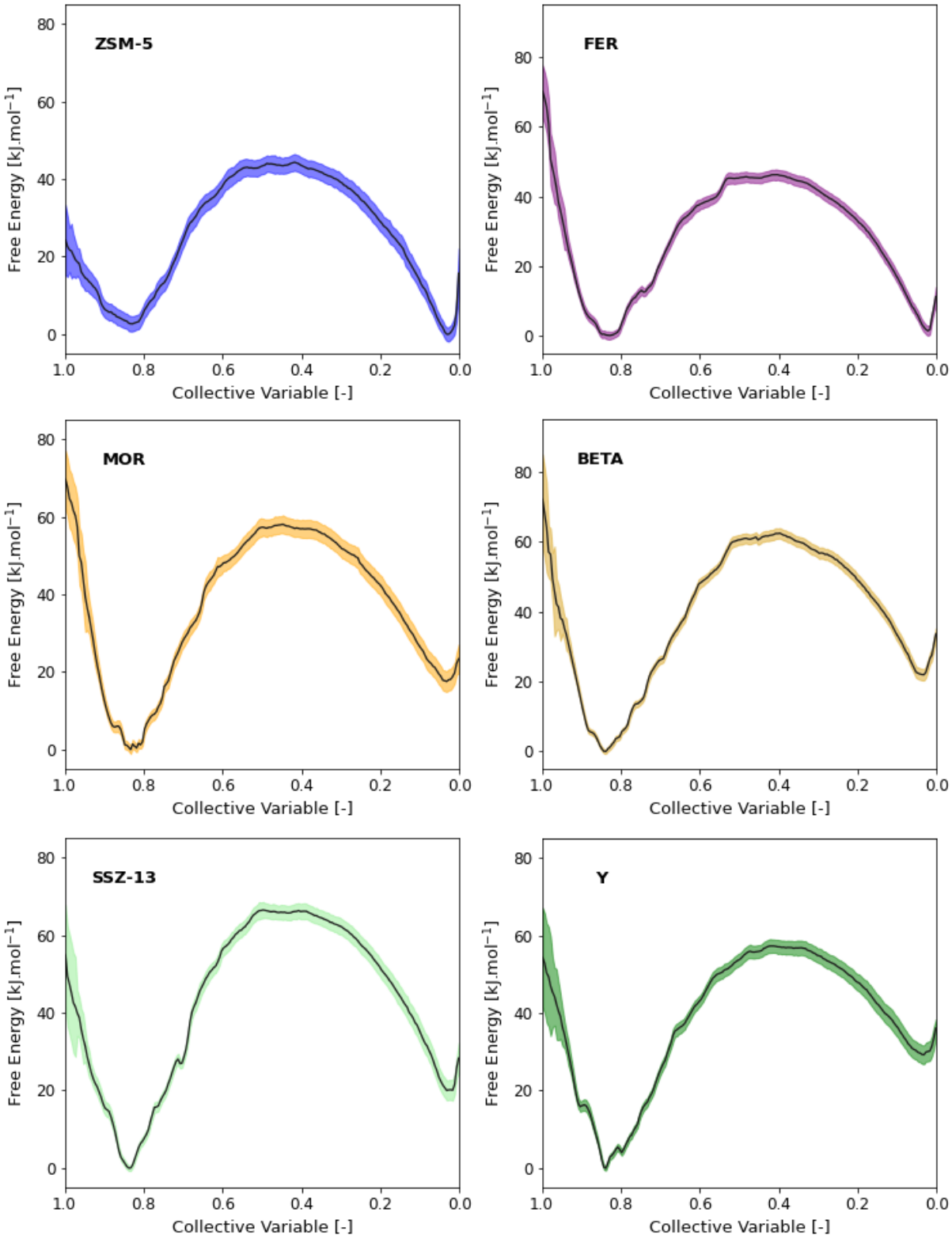

Figure S11. Free energy profiles at 773K for isobutene protonation into a tert-butyl carbenium ion in the multi-dimensional zeolite topologies ZSM-5, FER, MOR, β, SSZ-13 and Y with indication of the error bars (colored area) as obtained from the MLE method.

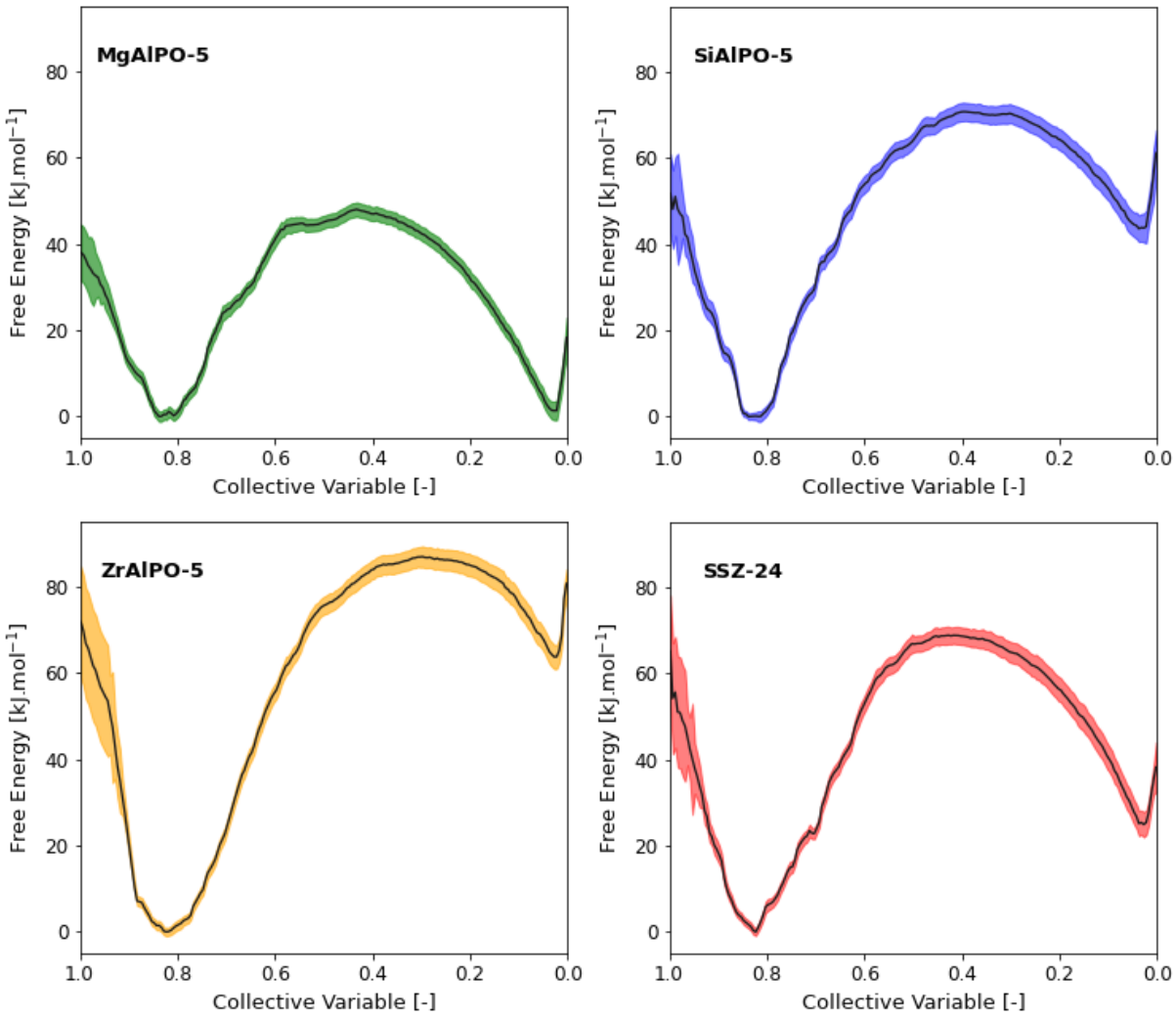

Figure S12. Free energy profiles at 773K for isobutene protonation into a tert-butyl carbenium ion in the AFI topologies with varying acid site strength MgAlPO-5, SiAlPO-5, ZrAlPO-5 and SSZ-24 with indication of the error bars (colored area) as obtained from the MLE method.

***Table S25*.** Phenomenological isobutene protonation barriers and reaction free energies at 773K for the different zeolite materials.

	$\Delta F^{\ddagger}_{phen}$ [kJ.mol^{-1}]	$\Delta F_{r,phen}$ [kJ.mol^{-1}]
H-ZSM-22	24.8	-2.3
H-SSZ-24	53.1	27.0
H-ITQ-4	49.8	23.1
H-DON	42.5	28.0
H-ZSM-5	31.1	2.5
H-FER	33.8	5.6
H-MOR	43.4	17.9
H-β	48.7	23.1
H-SSZ-13	50.6	20.5
H-Y	42.3	26.9
H-MgAlPO-5	35.2	5.0
H-SAPO-5	57.0	43.6
H-ZrAlPO-5	72.7	66.7

S7. Topology Descriptors

Due to the broad versatility in zeolite framework architectures, ranging from channel to cage topologies and from one-dimensional to three-dimensional topologies, it is far from trivial to identify a universal descriptor. A proper descriptor for adsorption properties should be capable to capture all intricate effects for the adsorbed intermediates, including covalent interactions, dispersion stabilization and entropic effects. Multiple possible descriptors have been previously suggested in literature to correlate the framework structure with their adsorption or catalytic behavior. These descriptors were typically either based on structural parameters (such as the available pore volume, pore limiting diameter or largest cavity diameter) or on thermodynamic properties (such as adsorption entropies or free energies of key model components).[46–54] Hereafter, we try if the proposed descriptors could be functional descriptors to predict trends in the adsorption behavior of the isobutene intermediates (isobutene π-complex and tert-butyl carbenium ion). **Figure S13** shows the performance of the maximum diameter of a sphere that can fit inside or diffuse along the pores of the framework (taken from the IZA database[1]) as topology descriptors. **Figure S14** shows the performance of the largest cavity diameter (LCD) or the pore limiting diameter (PLD), as determined by First et al.,[55] for the topology scaling relations. **Figure S15** illustrates the possible scaling relations with the available or occupiable pore volume by a probe sphere of 2.8 Å diameter of the framework topologies, as determined by Treacy and Foster.[56] **Figure S16** shows the correlation plots with the translational entropy of the physisorbed isobutene (from our US simulations) or the adsorption entropy of the tert-butyl carbenium ion at 773K (from our static calculations) as topology descriptors.

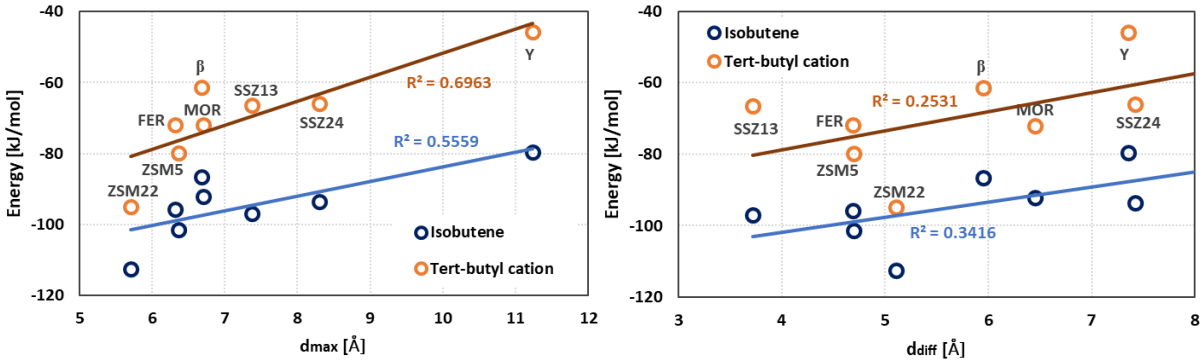

Figure S13. Scaling relations between the static isobutene π-complex and tert-butyl carbenium ion adsorption energies for the various topologies and the maximum diameter of a sphere that can fit inside the framework (left) or maximum diameter of a sphere that can diffuse along the main channel or through the pore windows of the framework (right), according to the IZA database.[1]

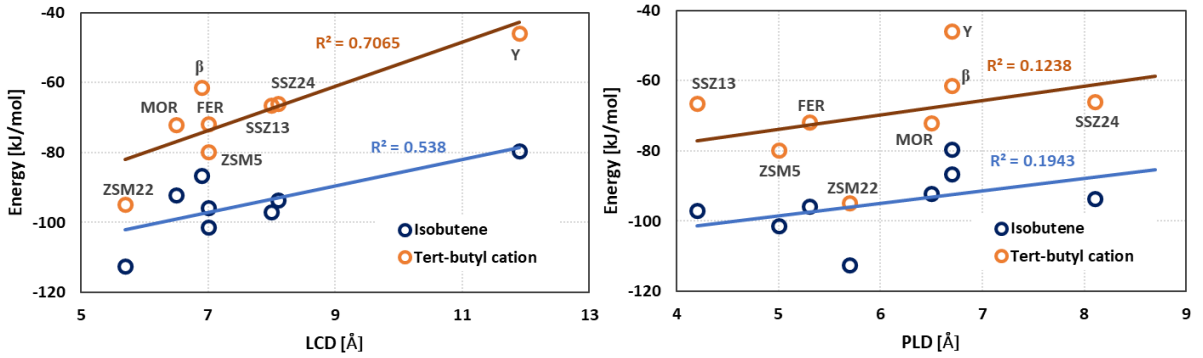

Figure S14. Scaling relations between the static isobutene π-complex and tert-butyl carbenium ion adsorption energies for the various topologies and the largest cavity diameter, LCD (left) or the pore limiting diameter, PLD (right), according to the study of First et al.[55]

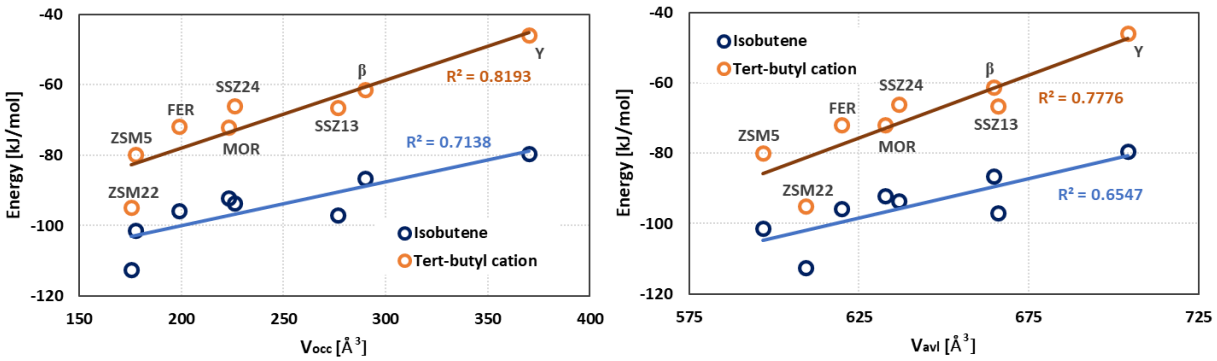

Figure S15. Scaling relations between the static isobutene π-complex and tert-butyl carbenium ion adsorption energies for the various topologies and the occupiable pore volume (left) or the available pore volume (right), according to the work of Treacy and Foster.[56]

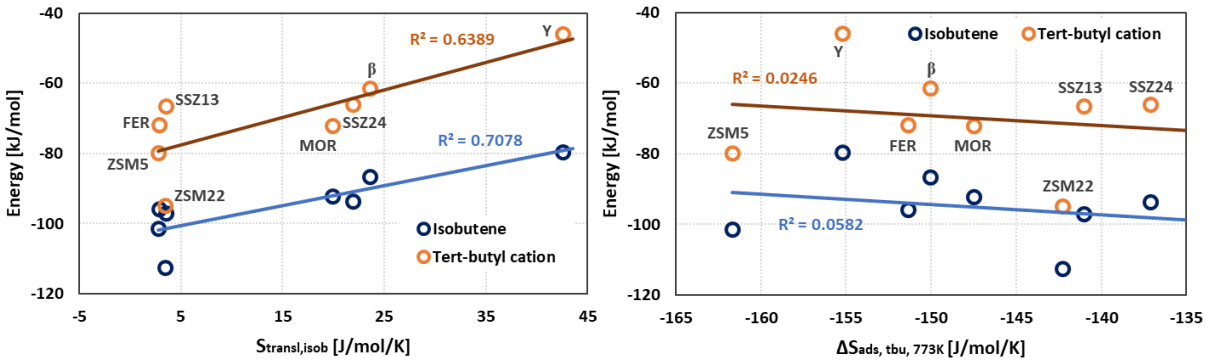

Figure S16. Scaling relations between the static isobutene π-complex and tert-butyl carbenium ion adsorption energies for the various topologies and the translational entropy of the physisorbed isobutene reactant from the US simulations at 773K (left) or the tert-butyl carbenium ion adsorption entropy at 773K from static calculations (right).

So far, none of these topology descriptors was very successful in predicting a clear correlation with the isobutene adsorption energies. Previously, Iglesia et al.[49] and Studt et al.[54] highlighted the importance of van der Waals contributions for the adsorption of alkenes and showed that the van der Waals energies can yield linear correlations with transition state energies for alkene conversions in different zeolite frameworks. Analogously, we suggest using the D3 dispersion component of the isobutene adsorption energies as possible descriptor for the adsorption of the isobutene intermediates. Since the magnitude of the D3 dispersion contribution to the static adsorption energies may show significant variations, depending on the specific orientation of the adsorbate, in particular for the large pore frameworks with high conformational freedom, we opted to compute the D3 dispersion in a different way. From the isobutene reactant windows in the US simulations at 773 K, 10 significantly different conformations of the physisorbed isobutene (both π-complex and vdW-complex states) were selected. For each of these conformations, a single-point calculation at the revPBE-D3 level of theory was carried out on (i) the framework with adsorbed isobutene, (ii) the empty framework with isobutene removed and also on (iii) isobutene in gas phase with the framework removed. From each single point calculation the Grimme D3 dispersion energy was deduced and the dispersion component of the isobutene adsorption energy was calculated. Ultimately, the average D3 dispersion energy of the 10 conformations was computed as the final estimate. **Table S26** summarizes the dispersion energies for all investigated frameworks. **Figure 2** in the main manuscript shows the performance of this descriptor for the static isobutene intermediates adsorption energies.

$$\Delta E_{disp-D3} = \frac{1}{10}\sum_{n=1}^{10}\left(E_{D3,\ Z-H+C_4H_8} - E_{D3,\ Z-H} - E_{D3,\ C_4H_8}\right)$$

***Table S26*.** Grimme D3 dispersion energy components, $\Delta E_{disp\text{-}D3}$ [kJ.mol^{-1}], to the isobutene adsorption energies, averaged from 10 different conformations.

Topology	$\Delta E_{disp\text{-}D3}$	
	Average [kJ.mol^{-1}]	**Standard deviation [kJ.mol^{-1}]**
ZSM-22	-75.82	1.74
SSZ-24	-52.85	3.58
ITQ-4	-54.65	3.63
DON	-48.15	5.06
ZSM-5	-73.26	7.07
FER	-72.79	2.52
MOR	-59.80	3.69
β	-55.72	4.68
SSZ-13	-57.88	4.75
Y	-37.35	6.02

S8. References

(1) *Database of Zeolite Structures. Http://Www.Iza-Structure.Org/ Databases/*; 2019.
(2) Moses, P. G.; Nørskov, J. K. Methanol to Dimethyl Ether over ZSM-22: A Periodic Density Functional Theory Study. *ACS Catal.* **2013**, *3* (4), 735–745. https://doi.org/10.1021/cs300722w.
(3) Brogaard, R. Y.; Wang, C.-M.; Studt, F. Methanol–Alkene Reactions in Zeotype Acid Catalysts: Insights from a Descriptor-Based Approach and Microkinetic Modeling. *ACS Catal.* **2014**, *4* (12), 4504–4509. https://doi.org/10.1021/cs5014267.
(4) Brändle, M.; Sauer, J. Acidity Differences between Inorganic Solids Induced by Their Framework Structure. A Combined Quantum Mechanics/Molecular Mechanics Ab Initio Study on Zeolites. *J. Am. Chem. Soc.* **1998**, *120* (7), 1556–1570. https://doi.org/10.1021/ja9729037.
(5) Nieminen, V.; Sierka, M.; Murzin, D. Yu.; Sauer, J. Stabilities of C3–C5 Alkoxide Species inside H-FER Zeolite: A Hybrid QM/MM Study. *J. Catal.* **2005**, *231* (2), 393–404. https://doi.org/10.1016/j.jcat.2005.01.035.
(6) Tuma, C.; Kerber, T.; Sauer, J. The Tert-Butyl Cation in H-Zeolites: Deprotonation to Isobutene and Conversion into Surface Alkoxides. *Angew. Chem. Int. Ed.* **2010**, *49* (27), 4678–4680. https://doi.org/10.1002/anie.200907015.
(7) De Moor, B. A.; Reyniers, M.-F.; Gobin, O. C.; Lercher, J. A.; Marin, G. B. Adsorption of C2-C8 n-Alkanes in Zeolites. *J. Phys. Chem. C* **2011**, *115* (4), 1204–1219. https://doi.org/10.1021/jp106536m.
(8) Hernandez-Tamargo, C.; O'Malley, A.; P. Silverwood, I.; Leeuw, N. H. de. Molecular Behaviour of Phenol in Zeolite Beta Catalysts as a Function of Acid Site Presence: A Quasielastic Neutron Scattering and Molecular Dynamics Simulation Study. *Catal. Sci. Technol.* **2019**, *9* (23), 6700–6713. https://doi.org/10.1039/C9CY01548E.
(9) Sierka, M.; Sauer, and J. Structure and Reactivity of Silica and Zeolite Catalysts by a Combined Quantum Mechanics[Ndash]Shell-Model Potential Approach Based on DFT. *Faraday Discuss.* **1997**, *106* (0), 41–62. https://doi.org/10.1039/A701492I.
(10) Vanpoucke, D. E. P.; Lejaeghere, K.; Van Speybroeck, V.; Waroquier, M.; Ghysels, A. Mechanical Properties from Periodic Plane Wave Quantum Mechanical Codes: The Challenge of the Flexible Nanoporous MIL-47(V) Framework. *J. Phys. Chem. C* **2015**, *119* (41), 23752–23766. https://doi.org/10.1021/acs.jpcc.5b06809.
(11) Denayer, J. F.; Baron, G. V.; Martens, J. A.; Jacobs, P. A. Chromatographic Study of Adsorption of N-Alkanes on Zeolites at High Temperatures. *J. Phys. Chem. B* **1998**, *102* (17), 3077–3081. https://doi.org/10.1021/jp972328t.
(12) Arik, I. C.; Denayer, J. F.; Baron, G. V. High-Temperature Adsorption of n-Alkanes on ZSM-5 Zeolites: Influence of the Si/Al Ratio and the Synthesis Method on the Low-Coverage Adsorption Properties. *Microporous Mesoporous Mater.* **2003**, *60* (1), 111–124. https://doi.org/10.1016/S1387-1811(03)00332-9.
(13) Mlinar, A. N.; Zimmerman, P. M.; Celik, F. E.; Head-Gordon, M.; Bell, A. T. Effects of Brønsted-Acid Site Proximity on the Oligomerization of Propene in H-MFI. *J. Catal.* **2012**, *288*, 65–73. https://doi.org/10.1016/j.jcat.2012.01.002.
(14) Kresse, G.; Hafner, J. Ab Initio Molecular Dynamics for Liquid Metals. *Phys. Rev. B* **1993**, *47* (1), 558–561. https://doi.org/10.1103/PhysRevB.47.558.
(15) Kresse, G.; Hafner, J. Ab Initio Molecular-Dynamics Simulation of the Liquid-Metal Amorphous-Semiconductor Transition in Germanium. *Phys. Rev. B* **1994**, *49* (20), 14251–14269. https://doi.org/10.1103/PhysRevB.49.14251.
(16) Kresse, G.; Furthmüller, J. Efficiency of Ab-Initio Total Energy Calculations for Metals and Semiconductors Using a Plane-Wave Basis Set. *Comput. Mater. Sci.* **1996**, *6* (1), 15–50. https://doi.org/10.1016/0927-0256(96)00008-0.
(17) Kresse, G.; Furthmüller, J. Efficient Iterative Schemes for Ab Initio Total-Energy Calculations Using a Plane-Wave Basis Set. *Phys. Rev. B* **1996**, *54* (16), 11169–11186. https://doi.org/10.1103/PhysRevB.54.11169.

(18) Kresse, G.; Joubert, D. From Ultrasoft Pseudopotentials to the Projector Augmented-Wave Method. *Phys. Rev. B* **1999**, *59* (3), 1758–1775. https://doi.org/10.1103/PhysRevB.59.1758.
(19) Blöchl, P. E. Projector Augmented-Wave Method. *Phys. Rev. B* **1994**, *50* (24), 17953–17979. https://doi.org/10.1103/PhysRevB.50.17953.
(20) Perdew, J. P.; Burke, K.; Ernzerhof, M. Generalized Gradient Approximation Made Simple. *Phys. Rev. Lett.* **1996**, *77* (18), 3865–3868. https://doi.org/10.1103/PhysRevLett.77.3865.
(21) Grimme, S.; Antony, J.; Ehrlich, S.; Krieg, H. A Consistent and Accurate Ab Initio Parametrization of Density Functional Dispersion Correction (DFT-D) for the 94 Elements H-Pu. *J. Chem. Phys.* **2010**, *132* (15), 154104. https://doi.org/10.1063/1.3382344.
(22) Lejaeghere, K.; Bihlmayer, G.; Björkman, T.; Blaha, P.; Blügel, S.; Blum, V.; Caliste, D.; Castelli, I. E.; Clark, S. J.; Corso, A. D.; Gironcoli, S. de; Deutsch, T.; Dewhurst, J. K.; Marco, I. D.; Draxl, C.; Dułak, M.; Eriksson, O.; Flores-Livas, J. A.; Garrity, K. F.; Genovese, L.; Giannozzi, P.; Giantomassi, M.; Goedecker, S.; Gonze, X.; Grånäs, O.; Gross, E. K. U.; Gulans, A.; Gygi, F.; Hamann, D. R.; Hasnip, P. J.; Holzwarth, N. a. W.; Iuşan, D.; Jochym, D. B.; Jollet, F.; Jones, D.; Kresse, G.; Koepernik, K.; Küçükbenli, E.; Kvashnin, Y. O.; Locht, I. L. M.; Lubeck, S.; Marsman, M.; Marzari, N.; Nitzsche, U.; Nordström, L.; Ozaki, T.; Paulatto, L.; Pickard, C. J.; Poelmans, W.; Probert, M. I. J.; Refson, K.; Richter, M.; Rignanese, G.-M.; Saha, S.; Scheffler, M.; Schlipf, M.; Schwarz, K.; Sharma, S.; Tavazza, F.; Thunström, P.; Tkatchenko, A.; Torrent, M.; Vanderbilt, D.; Setten, M. J. van; Speybroeck, V. V.; Wills, J. M.; Yates, J. R.; Zhang, G.-X.; Cottenier, S. Reproducibility in Density Functional Theory Calculations of Solids. *Science* **2016**, *351* (6280), aad3000. https://doi.org/10.1126/science.aad3000.
(23) Ghysels, A.; Neck, D. V.; Speybroeck, V. V.; Verstraelen, T.; Waroquier, M. Vibrational Modes in Partially Optimized Molecular Systems. *J. Chem. Phys.* **2007**, *126* (22), 224102. https://doi.org/10.1063/1.2737444.
(24) Reetz, M. T.; Meiswinkel, A.; Mehler, G.; Angermund, K.; Graf, M.; Thiel, W.; Mynott, R.; Blackmond, D. G. Why Are BINOL-Based Monophosphites Such Efficient Ligands in Rh-Catalyzed Asymmetric Olefin Hydrogenation? *J. Am. Chem. Soc.* **2005**, *127* (29), 10305–10313. https://doi.org/10.1021/ja052025+.
(25) Donoghue, P. J.; Helquist, P.; Norrby, P.-O.; Wiest, O. Development of a Q2MM Force Field for the Asymmetric Rhodium Catalyzed Hydrogenation of Enamides. *J. Chem. Theory Comput.* **2008**, *4* (8), 1313–1323. https://doi.org/10.1021/ct800132a.
(26) Ghysels, A.; Verstraelen, T.; Hemelsoet, K.; Waroquier, M.; Van Speybroeck, V. TAMkin: A Versatile Package for Vibrational Analysis and Chemical Kinetics. *J. Chem. Inf. Model.* **2010**, *50* (9), 1736–1750. https://doi.org/10.1021/ci100099g.
(27) VandeVondele, J.; Krack, M.; Mohamed, F.; Parrinello, M.; Chassaing, T.; Hutter, J. QUICKSTEP: Fast and Accurate Density Functional Calculations Using a Mixed Gaussian and Plane Waves Approach. *Comput. Phys. Commun.* **2005**, *167* (2), 103–128. https://doi.org/10.1016/j.cpc.2004.12.014.
(28) Zhang, Y.; Yang, W. Comment on ``Generalized Gradient Approximation Made Simple''. *Phys. Rev. Lett.* **1998**, *80* (4), 890–890. https://doi.org/10.1103/PhysRevLett.80.890.
(29) Goedecker, S.; Teter, M.; Hutter, J. Separable Dual-Space Gaussian Pseudopotentials. *Phys. Rev. B* **1996**, *54* (3), 1703–1710. https://doi.org/10.1103/PhysRevB.54.1703.
(30) Hartwigsen, C.; Goedecker, S.; Hutter, J. Relativistic Separable Dual-Space Gaussian Pseudopotentials from H to Rn. *Phys. Rev. B* **1998**, *58* (7), 3641–3662. https://doi.org/10.1103/PhysRevB.58.3641.
(31) Lippert, G.; Hutter, J.; Parrinello, M. A Hybrid Gaussian and Plane Wave Density Functional Scheme. *Mol. Phys.* **1997**, *92* (3), 477–488. https://doi.org/10.1080/002689797170220.
(32) Lippert, G.; Hutter, J.; Parrinello, M. The Gaussian and Augmented-Plane-Wave Density Functional Method for Ab Initio Molecular Dynamics Simulations. *Theor. Chem. Acc.* **1999**, *103* (2), 124–140. https://doi.org/10.1007/s002140050523.

(33) VandeVondele, J.; Hutter, J. Gaussian Basis Sets for Accurate Calculations on Molecular Systems in Gas and Condensed Phases. *J. Chem. Phys.* **2007**, *127* (11), 114105. https://doi.org/10.1063/1.2770708.
(34) Nosé, S. A Molecular Dynamics Method for Simulations in the Canonical Ensemble. *Mol. Phys.* **1984**, *52* (2), 255–268. https://doi.org/10.1080/00268978400101201.
(35) Martyna, G. J.; Klein, M. L.; Tuckerman, M. Nosé–Hoover Chains: The Canonical Ensemble via Continuous Dynamics. *J. Chem. Phys.* **1992**, *97* (4), 2635–2643. https://doi.org/10.1063/1.463940.
(36) Cnudde, P.; De Wispelaere, K.; Van der Mynsbrugge, J.; Waroquier, M.; Van Speybroeck, V. Effect of Temperature and Branching on the Nature and Stability of Alkene Cracking Intermediates in H-ZSM-5. *J. Catal.* **2017**, *345*, 53–69. https://doi.org/10.1016/j.jcat.2016.11.010.
(37) Torrie, G. M.; Valleau, J. P. Monte Carlo Free Energy Estimates Using Non-Boltzmann Sampling: Application to the Sub-Critical Lennard-Jones Fluid. *Chem. Phys. Lett.* **1974**, *28* (4), 578–581. https://doi.org/10.1016/0009-2614(74)80109-0.
(38) Torrie, G. M.; Valleau, J. P. Nonphysical Sampling Distributions in Monte Carlo Free-Energy Estimation: Umbrella Sampling. *J. Comput. Phys.* **1977**, *23* (2), 187–199. https://doi.org/10.1016/0021-9991(77)90121-8.
(39) Tribello, G. A.; Bonomi, M.; Branduardi, D.; Camilloni, C.; Bussi, G. PLUMED 2: New Feathers for an Old Bird. *Comput. Phys. Commun.* **2014**, *185* (2), 604–613. https://doi.org/10.1016/j.cpc.2013.09.018.
(40) ThermoLIB | Center for Molecular Modeling. Https://Molmod.Ugent.Be/Software/Thermolib.
(41) Bučko, T.; Chibani, S.; Paul, J.-F.; Cantrel, L.; Badawi, M. Dissociative Iodomethane Adsorption on Ag-MOR and the Formation of AgI Clusters: An Ab Initio Molecular Dynamics Study. *Phys. Chem. Chem. Phys.* **2017**, *19* (40), 27530–27543. https://doi.org/10.1039/C7CP05562E.
(42) Bailleul, S.; Dedecker, K.; Cnudde, P.; Vanduyfhuys, L.; Waroquier, M.; Van Speybroeck, V. Ab Initio Enhanced Sampling Kinetic Study on MTO Ethene Methylation Reaction. *J. Catal.* **2020**, *388*, 38–51. https://doi.org/10.1016/j.jcat.2020.04.015.
(43) Zhu, F.; Hummer, G. Convergence and Error Estimation in Free Energy Calculations Using the Weighted Histogram Analysis Method. *J. Comput. Chem.* **2012**, *33* (4), 453–465. https://doi.org/10.1002/jcc.21989.
(44) Bocus, M.; Vanduyfhuys, L.; De Proft, F.; Weckhuysen, B. M.; Van Speybroeck, V. Mechanistic Characterization of Zeolite-Catalyzed Aromatic Electrophilic Substitution at Realistic Operating Conditions. *JACS Au* **2022**, *2* (2), 502–514. https://doi.org/10.1021/jacsau.1c00544.
(45) Cnudde, P.; De Wispelaere, K.; Vanduyfhuys, L.; Demuynck, R.; Van der Mynsbrugge, J.; Waroquier, M.; Van Speybroeck, V. How Chain Length and Branching Influence the Alkene Cracking Reactivity on H-ZSM-5. *ACS Catal.* **2018**, *8* (10), 9579–9595. https://doi.org/10.1021/acscatal.8b01779.
(46) Van der Mynsbrugge, J.; Janda, A.; Mallikarjun Sharada, S.; Lin, L.-C.; Van Speybroeck, V.; Head-Gordon, M.; Bell, A. T. Theoretical Analysis of the Influence of Pore Geometry on Monomolecular Cracking and Dehydrogenation of N-Butane in Brønsted Acidic Zeolites. *ACS Catal.* **2017**, *7* (4), 2685–2697. https://doi.org/10.1021/acscatal.6b03646.
(47) Janda, A.; Vlaisavljevich, B.; Lin, L.-C.; Smit, B.; Bell, A. T. Effects of Zeolite Structural Confinement on Adsorption Thermodynamics and Reaction Kinetics for Monomolecular Cracking and Dehydrogenation of N-Butane. *J. Am. Chem. Soc.* **2016**, *138* (14), 4739–4756. https://doi.org/10.1021/jacs.5b11355.
(48) Janda, A.; Vlaisavljevich, B.; Smit, B.; Lin, L.-C.; Bell, A. T. Effects of Pore and Cage Topology on the Thermodynamics of N-Alkane Adsorption at Brønsted Protons in Zeolites at High Temperature. *J. Phys. Chem. C* **2017**, *121* (3), 1618–1638. https://doi.org/10.1021/acs.jpcc.6b09703.
(49) Sarazen, M. L.; Doskocil, E.; Iglesia, E. Catalysis on Solid Acids: Mechanism and Catalyst Descriptors in Oligomerization Reactions of Light Alkenes. *J. Catal.* **2016**, *344*, 553–569. https://doi.org/10.1016/j.jcat.2016.10.010.

(50) Chen, Y.; Zhao, X.; Qin, Z.; Wang, S.; Wei, Z.; Li, J.; Dong, M.; Wang, J.; Fan, W. Insight into the Methylation of Alkenes and Aromatics with Methanol over Zeolite Catalysts by Linear Scaling Relations. *J. Phys. Chem. C* **2020**, *124* (25), 13789–13798. https://doi.org/10.1021/acs.jpcc.0c03405.
(51) Latimer, A. A.; Kulkarni, A. R.; Aljama, H.; Montoya, J. H.; Yoo, J. S.; Tsai, C.; Abild-Pedersen, F.; Studt, F.; Nørskov, J. K. Understanding Trends in C–H Bond Activation in Heterogeneous Catalysis. *Nat. Mater.* **2017**, *16* (2), 225–229. https://doi.org/10.1038/nmat4760.
(52) Gu, Y.; Liu, Z.; Yu, C.; Gu, X.; Xu, L.; Gao, Y.; Ma, J. Zeolite Adsorption Isotherms Predicted by Pore Channel and Local Environmental Descriptors: Feature Learning on DFT Binding Strength. *J. Phys. Chem. C* **2020**, *124* (17), 9314–9328. https://doi.org/10.1021/acs.jpcc.0c00130.
(53) Kang, J. H.; Alshafei, F. H.; Zones, S. I.; Davis, M. E. Cage-Defining Ring: A Molecular Sieve Structural Indicator for Light Olefin Product Distribution from the Methanol-to-Olefins Reaction. *ACS Catal.* **2019**, *9* (7), 6012–6019. https://doi.org/10.1021/acscatal.9b00746.
(54) Fečík, M.; Plessow, P. N.; Studt, F. Influence of Confinement on Barriers for Alkoxide Formation in Acidic Zeolites. *ChemCatChem* **2021**, *13* (10), 2451–2458. https://doi.org/10.1002/cctc.202100009.
(55) L. First, E.; E. Gounaris, C.; Wei, J.; A. Floudas, C. Computational Characterization of Zeolite Porous Networks: An Automated Approach. *Phys. Chem. Chem. Phys.* **2011**, *13* (38), 17339–17358. https://doi.org/10.1039/C1CP21731C.
(56) Treacy, M. M. J.; Foster, M. D. Packing Sticky Hard Spheres into Rigid Zeolite Frameworks. *Microporous Mesoporous Mater.* **2009**, *118* (1), 106–114. https://doi.org/10.1016/j.micromeso.2008.08.039.